



Sulfur from the subducted slab dominates the sulfur budget of the mantle wedge under volcanic arcs

Z. Taracsák^{a,*}, T.A. Mather^a, S. Ding^b, T. Plank^b, M. Brounce^c, D.M. Pyle^a, A. Aiuppa^d, EIMF^e

^a Department of Earth Sciences, University of Oxford, Oxford OX1 3AN, United Kingdom

^b Lamont Doherty Earth Observatory, Columbia University, Palisades, NY 10964-8000, United States of America

^c Department of Earth and Planetary Sciences, University of California Riverside, Riverside, CA 92521, United States of America

^d Dipartimento di Scienze Della Terra e Del Mare, Università degli Studi di Palermo, 90123 Palermo, Italy

^e Edinburgh Ion Microprobe Facility, School of GeoSciences, University of Edinburgh, James Hutton Road, Edinburgh EH9 3FE, United Kingdom

ARTICLE INFO

Article history:

Received 18 August 2022

Received in revised form 2 December 2022

Accepted 4 December 2022

Available online 16 December 2022

Editor: C.M. Petrone

Keywords:

sulfur isotopes

melt inclusions

Central American volcanic arc

mantle wedge

sulfur degassing

ABSTRACT

Sulfur is of a crucial importance in the Earth system influencing biological, climate, ore-forming, and redox processes. Subduction zones play a key role in the global sulfur cycle. Arc magmas have higher sulfur contents and are more oxidised than mid-ocean ridge basalts (MORBs) due to either an oxidised mantle source or magma differentiation. Melt oxidation state and sulfur content may interrelate, as sulfur is a potential oxidising agent during slab-mantle interaction. Here, we use melt inclusions (MIs) to determine the sulfur isotopic composition ($\delta^{34}\text{S}$) of primary arc magmas from three volcanic centres along the Central American Volcanic Arc (CAVA): Fuego (Guatemala), Cerro Negro (Nicaragua), and Turrialba (Costa Rica). These three locations sample much of the global arc magma trace element variability: Ba/La ratios range from 22 (Turrialba) to 118 (Cerro Negro). Melt $\delta^{34}\text{S}$ values are between -0.5‰ and $+4.9\text{‰}$. Sulfur contents and $\delta^{34}\text{S}$ values of homogenised and naturally quenched MIs overlap, indicating post-entrapment processes do not affect sulfur contents and sulfur isotope ratios in the studied MIs. Degassing causes limited sulfur isotope fractionation; calculated gas-melt isotope fractionation factors are between 0.998–1.001. Our model calculations predict that most volcanic gases along the CAVA have $\delta^{34}\text{S}$ between -1‰ and $+6\text{‰}$, becoming enriched in ^{34}S as degassing progresses. We estimate initial melt $\delta^{34}\text{S}$ values for Fuego, Cerro Negro, and Turrialba to be $+0.7\pm 1.4\text{‰}$, $+2.2\pm 1.0\text{‰}$, and $+1.6\pm 0.8\text{‰}$ (two standard errors), respectively. All these values are elevated compared to MORBs (-0.9‰). Addition of oxidised slab material enriched in ^{34}S to the mantle wedge can explain elevated arc primary melt $\delta^{34}\text{S}$ and the oxidising conditions observed in arc magmas globally. Based on mass balance, a slab component with $\delta^{34}\text{S}$ between $+2\text{‰}$ to $+5\text{‰}$ is present in the mantle wedge under the CAVA, elevating local arc mantle S contents to 360 ± 30 ppm at Fuego, 462 ± 11 ppm at Cerro Negro. Modelling suggests that 40–70% of sulfur in the mantle wedge originates from a slab-derived component. Slab subduction is expected to have major control on the evolution of Earth's sulfur cycle and mantle oxidation state over its geological history.

© 2022 The Author(s). Published by Elsevier B.V. This is an open access article under the CC BY license (<http://creativecommons.org/licenses/by/4.0/>).

1. Introduction

Arc magmatism is driven by interactions between the subducting slab and the overlying mantle. Slabs transport volatile-rich and oxidising surface material, such as sedimentary and hydrothermally-altered lithologies, into the mantle, where these undergo partial de-volatilisation as they subduct (e.g. Schmidt and

Poli, 2014). Interactions between the subducting slab, overlying mantle, volcanic arcs, and the Earth's surface are of fundamental importance to the geochemical cycle of elements, including volatiles (e.g. Bekaert et al., 2021), and to Earth's redox evolution over geological timescales (e.g. Stolper et al., 2021).

Sulfur is a volatile element that can be present in variable valence states at oxygen fugacity ($f\text{O}_2$) conditions relevant to metamorphic (e.g. Walters et al., 2020) and igneous (e.g. Jugo et al., 2010; Nash et al., 2019) processes on Earth. This property makes sulfur an important electron donor or acceptor, alongside iron and carbon, in geological systems (Mungall, 2002; Evans, 2012).

* Corresponding author.

E-mail address: zoltan.taracsak@earth.ox.ac.uk (Z. Taracsák).

Arc magmas contain more sulfur than mid-ocean ridge basalts (MORBs), the former reaching >4000 ppm (Muth and Wallace, 2021). They are also more oxidised than MORBs, with arc magma fO_2 measured >1 log unit above the fayalite-magnetite-quartz buffer (Brounce et al., 2014; Muth and Wallace, 2022). These observations, alongside correlations between melt redox proxies (such as $Fe^{3+}/\Sigma Fe$) and ratios of Ba/La (Brounce et al., 2014), Sr/Nd, and S/Dy (Muth and Wallace, 2021, 2022) have been interpreted to indicate that the mantle wedge under volcanic arcs is more oxidised than the depleted MORB mantle (DMM). Slab-derived sulfur originating from the altered oceanic crust, serpentines, and seawater carried by the slab has been proposed as a driver of oxidation in the mantle wedge (Walters et al., 2020; Muth and Wallace, 2021; de Moor et al., 2022) and elevated S contents measured in arc magmas (Kawaguchi et al., 2022). Arguments for inherently oxidised arc magmas have been questioned based on their transition metal contents (e.g. Lee et al., 2012), although the use of transition metal melting models as a proxy of low fO_2 in primary arc magmas is contentious (e.g. Stolper and Bucholz, 2019; Zhao et al., 2022). Alternative explanations of elevated fO_2 and S contents observed in arc magmas include post-melting differentiation (e.g. Tassara et al., 2020) and assimilation of sulfur from the lower crust or upper mantle (Lee et al., 2012, 2018). Oxidising conditions in arc magmas have been linked to H_2O dissociation during melt transport in the mantle (Tollan and Hermann, 2019).

The transfer of sulfur from subducting slabs to volcanic arcs can influence redox conditions on Earth's surface and in its mantle over geological timescales (e.g. Evans, 2012). Yet, questions remain about how much sulfur is added from the subducting slab into the mantle wedge, and whether it is oxidised or reduced (Jégo and Dasgupta, 2014; Muth and Wallace, 2021). Biological, sedimentary, and hydrothermal processes add sulfur to the oceanic lithosphere and fractionate sulfur isotopes. Minerals and lithologies form within the oceanic lithosphere (the downgoing slab) with distinct isotopic composition: sedimentary pyrite (reaching $\delta^{34}S < -40\text{‰}$, relative to V-CDT), seawater-derived sulfate ($\delta^{34}S$ up to +23‰, Canfield, 2004), pristine oceanic crust (near -1‰, Labidi et al., 2012) and serpentinite (+5‰ to +10‰, Alt and Shanks, 2003). The sulfur isotopic composition of slab-derived fluids and melts potentially reflect that of their origin, hence a slab component containing mostly oxidised sulfur may elevate $\delta^{34}S$ and fO_2 in the arc mantle source compared to DMM (Muth and Wallace, 2021; de Moor et al., 2022). Alternatively, sulfur isotopes may fractionate in slab fluids as they travel through the slab towards the mantle wedge, decoupling the isotopic composition of the slab fluid protolith and that of the slab fluid itself, which may also result in sulfate and ^{34}S enrichment in slab fluids that react with the upper mantle (Walters et al., 2019).

The sulfur isotopic composition of primitive arc magmas can provide insight into the subduction sulfur cycle. However, the determination of primary arc melt sulfur isotope composition is complicated by degassing in volcanic systems (e.g. de Hoog et al., 2001). New analytical developments now enable high-precision microanalyses of sulfur isotope ratios in volcanic glasses, such as melt inclusions (MIs), by secondary ion mass spectrometry (SIMS, Muth and Wallace 2021; Taracsák et al. 2021). The measurement of permil-level variations in $\delta^{34}S$ values allows correction for degassing processes, which is important in identifying variations in the sulfur isotopic composition of mantle-derived magmas. By directly analysing $\delta^{34}S$ in glasses we can investigate whether isotope ratios measured in volcanic gases faithfully record the composition of mantle-derived melts (e.g. de Moor et al., 2022), and whether melt $\delta^{34}S$ is a reliable global proxy of arc magma oxidation state (Muth and Wallace, 2021).

Here we use new SIMS procedures to determine for the first time the sulfur isotope composition of olivine-hosted MIs, both

highly and minimally degassed, from the Central American volcanic arc (CAVA). We use data from three volcanoes that cover much of the along-strike geochemical variability observed in the CAVA (Patino et al., 2000; Bolge et al., 2009; Carr et al., 2015) and in primitive arc magmas globally (Ruscitto et al., 2012): Volcán de Fuego (Guatemala), Cerro Negro (Nicaragua), and Turrialba (Costa Rica, Fig. 1). We use the new $\delta^{34}S$ data together with measurements of $S^{6+}/\Sigma S$ ratios via S-X-ray absorption near edge structure spectroscopy (S-XANES), measured from a subset of MIs, and literature trace element and $\delta^{34}S$ data to investigate the potential relationship between the high sulfur contents measured in arc magmas and slab-mantle interactions. Using our data, we model the S isotope composition of slab fluids/melts and the S content of the subarc mantle. We investigate whether $\delta^{34}S$ values in undegassed arc melts and slab fluids/melts correlate with tracers of slab-mantle interaction (i.e. Ba/La, Sr/Nd) and primary arc melt fO_2 , as observed in southern Cascadia (Muth and Wallace, 2021). We use our data to constrain sulfur isotope fractionation factors during volcanic degassing, which provide crucial insight into the interpretation of volcanic gas $\delta^{34}S$. We investigate the relationship between melt $\delta^{34}S$ values and those measured in volcanic gases from the same arc system (de Moor et al., 2022).

2. Geological background

The CAVA forms a >1000 km volcanic front stretching from the Mexico-Guatemala border to central Costa Rica (Fig. 1A). It lies between 100 and 180 km behind the Central American trench. The Cocos Plate is moving toward the Caribbean Plate at a rate of 50–65 mm/year, resulting in the fast subduction of 26 and 16 Ma oceanic plate under Guatemala to Nicaragua and Costa Rica, respectively (Müller et al., 2008). Thermal models indicate that maximum mantle wedge temperature and slab temperature is $\sim 200^\circ\text{C}$ lower under Costa Rica than under Guatemala and Nicaragua (Syracuse et al., 2010).

The extensive geochemical data collected from Quaternary CAVA volcanics (Carr et al., 2015) show highly variable trace element compositions: Ba/La and La/Yb ratios change by one order of magnitude along the length of the arc (Fig. 1B,C). Trace element ratio variability along the CAVA encompasses much of the global variation observed in primitive arc magmas (Ruscitto et al., 2012). This variability has been interpreted variously to reflect the changing contribution of slab-derived fluids to the mantle wedge (Patino et al., 2000), changes in slab depth beneath the various arc segments, changing melting degree (Bolge et al., 2009), melting in the lithospheric mantle under Costa Rica (Leeman et al., 1994), introduction of an enriched mantle component via northward mantle flow (Herrstrom et al., 1995), mantle heterogeneity (Heydolph et al., 2012, and references therein), and arc-hotspot interaction caused by the subduction of Cocos Ridge seamounts and oceanic crust with ocean island provenance (high incompatible trace element content, radiogenic Pb isotopic composition, Benjamin et al. 2007; Hoernle et al. 2008; Gazel et al. 2009). Here we focus on three volcanic centres: Volcán de Fuego (Guatemala), Cerro Negro (Nicaragua), and Turrialba (Costa Rica), which together record much of the along-strike geochemical variability at the CAVA (Fig. 1).

3. Samples and methods

We use three, crystal-rich scoria samples: sample VF18-AC4 from Fuego (provided by Omar Flores, Universidad San Carlos), a tephra fall deposit from the 2018 eruption (Shi et al., 2021), sample CN16ACB3B from Cerro Negro, a mafic tephra erupted in 1995 (Barth et al., 2019), and TURRI1865-A7 from Turrialba, a mafic scoriaceous lapilli sample from the 1864–1866 eruption (provided by

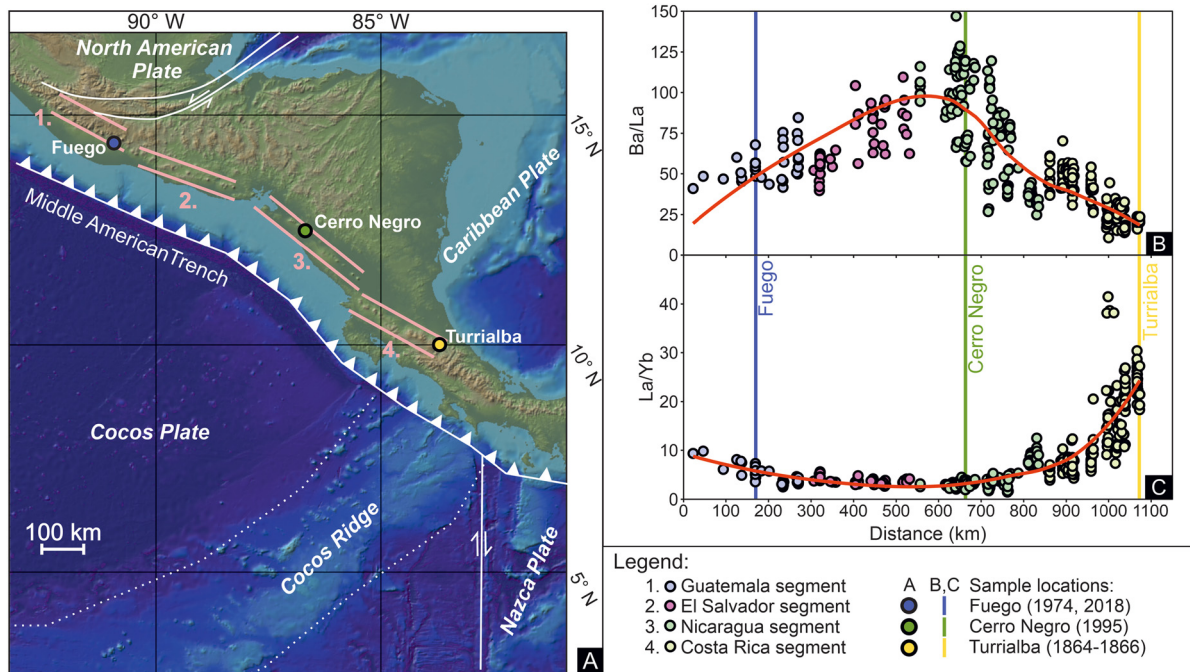


Fig. 1. (A) Map of the Central American Volcanic Arc (CAVA). Topographic/bathymetric base for the map was created using GeoMapApp (<https://www.geomapp.org/>). Numbered, parallel pink lines indicate segments of the CAVA (1: Guatemala; 2: El Salvador; 3: Nicaragua; 4: Costa Rica). Along-strike compositional variability of CAVA whole rock samples in Ba/La (B) and (C) in La/Yb; data from Carr et al., 2015). Along arc distance presented on the x-axis in (B,C) is measured from the northwestern terminus of the CAVA at the Guatemala-Mexico border. Coloured vertical lines indicate the along-strike position of the studied volcanoes. For interpretation of the colours in the figures, the reader is referred to the web version of this article.

Maarten de Moor, Universidad Nacional). Further detail is provided in the supplementary material.

To investigate the potential effects of post-entrapment crystallisation (PEC) or melting (PEM; Fig. 2) on sulfur concentrations and the isotopic composition of MIs, for example by sulfide formation in response to diffusive Fe-loss (Danyushevsky et al., 2002) and sulfide/sulfate formation along the bubble glass interface (Schiavi et al., 2020), we carried out analyses on a set of re-homogenised olivine-hosted MIs from Cerro Negro and Fuego alongside the naturally-quenched MIs. These inclusions were re-homogenised under high-pressure and temperature using a piston cylinder following procedures described by (Rasmussen et al., 2020). Further detail is provided in the supplementary material.

Major- and minor element, Cl, and S contents in glasses and inclusion host crystals were determined using a Cameca SXFive electron probe microanalyser at the University of Oxford using variable beam currents (4, 10, 40, and 100 nA) and an accelerating voltage of 15 kV (see supplementary material for further details).

Volatile elements, Li, B, and P were analysed by secondary ion mass spectrometry (SIMS) at the Edinburgh Ion Microprobe Facility (EIMF) using a Cameca IMS-1270 and a Cameca 7f-geo. Fluorine, S, Cl, and P were measured using a Cs^+ beam on the IMS-1270, while H, C, Li and B were analysed using an O^- beam on the 7f-geo (see supplementary material for further details).

Sulfur speciation was determined on a subset of the glasses using synchrotron micro-x-ray absorption near-edge spectroscopy (μXANES). Spectra were collected using beam line 13-IDE at the Advanced Photon Source, Argonne National Laboratory (see supplementary material for further details).

Sulfur isotope analyses of glasses were carried out at EIMF in November 2020 and February 2022 using a Cameca IMS-1270, following the analytical procedures detailed in (Taracsák et al., 2021). Sulfur isotope ratios were measured in multi-collector mode using a Cs^+ primary beam with a 10 μm diameter, a beam current between 3 and 5.5 nA, a primary accelerating voltage of 10 kV, and a mass resolution of 4800. We used a set of eight glass calibration

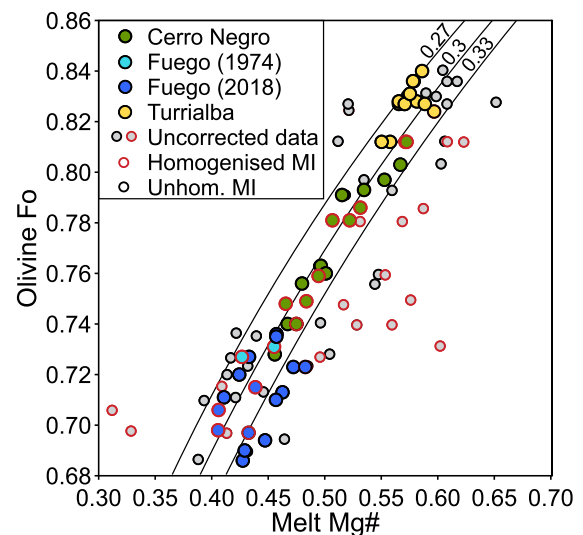


Fig. 2. Olivine forsterite content (Fo) vs. melt magnesium-number diagram showing both the uncorrected (grey filled) and PEC/PEM corrected (blue, green, and yellow symbols) composition of the studied olivine-hosted CAVA melt inclusions. Symbols with red outlines are experimentally re-homogenised MIs. Solid lines indicate the canonical value of the olivine-melt (Mg-Fe) partition coefficient ($K(d)_{\text{ol-melt}}^{\text{Fe-Mg}}$) at 0.3 ± 0.03 (Putirka, 2008). Details on how PEC/PEM correction was carried out on our dataset are provided in the supplementary material.

standards (Taracsák et al., 2021) to characterise potential instrumental mass fractionation (IMF) for our S isotope ratio analyses. These standards have sulfur contents between 530 and 3450 ppm and cover a compositional range from picobasalt to rhyolite.

During analysis we found evidence of significant IMF. Regression analysis shows that IMF correlates strongly with the sulfur content of the glass standards. Instrumental mass fractionation observed in 2022 was similar to that in Taracsák et al. (2021); IMF was more limited in 2020.

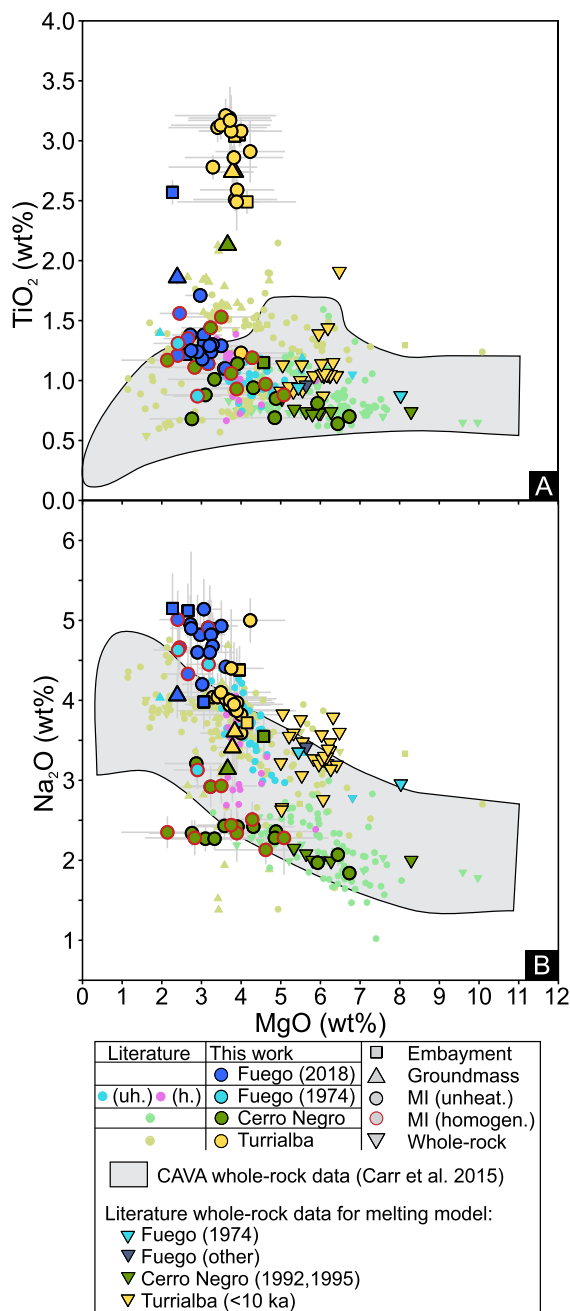


Fig. 3. Major element composition of studied CAVA glasses on TiO_2 vs MgO (A) and Na_2O vs MgO (B) plots. Gray fields indicate the compositional range covered by CAVA whole-rock samples (Carr et al., 2015). Small symbols are literature data from the studied volcanoes, including whole-rock samples (downward triangles - larger downward triangles represent whole rock data used for melting degree modelling in our discussion), MLs (circles) and matrix glass data (triangles). Cerro Negro literature data are from Barth et al. (2019); unhomogenised (uh.) Fuego 1974 (light blue) data are from Lloyd et al. (2013) and Rasmussen et al. (2020); homogenised (h., pink) Fuego 1974 melt inclusion data are from Rasmussen et al. (2020); data for Turrialba are from de Moor et al. (2016). Error bars are 2σ errors given by the MIMic software for PEC/PEM corrected inclusions; for all other samples EPMA analytical errors are plotted.

Correction for IMF was carried out using a linear S content-based regression for unknown data collected in 2020 and a $\ln(S)$ regression for data collected in 2022, which eliminates IMF for $\sim 80\%$ of standard analyses within a 2σ uncertainty of their bulk sulfur isotope composition (see supplementary material for details on error definitions).

Our observations regarding IMF differ from those published by Muth and Wallace (2021), who measured statistically insignificant IMF during glass sulfur isotope ratio analyses by SIMS. Their analyses used a different analytical setup (lower primary beam current, single collection using one electron multiplier detector) and standard set. The cause of these contrasting observations is not yet understood, and highlights the importance of using multiple calibration standards with variable S contents during S isotope analyses in glasses by SIMS (see supplementary material for further details on sulfur isotope analyses and IMF correction).

4. Results

4.1. Major, trace, and volatile elements

Major element compositions of studied glasses and inclusion hosts generally overlap with published whole-rock, MI, and glass data (Figs. 2, 3, supplementary Fig. S1). Glass compositions vary from basaltic to trachyandesitic. Turrialba samples have high incompatible major and minor elements contents, including TiO_2 (2.5–3.2 wt%) and P_2O_5 (0.8–1.0 wt%), which are uniformly higher than samples from the same eruption (de Moor et al., 2016), but overlap with the high-Nb Turrialba samples (Reagan and Gill, 1989; DeVitre et al., 2019). Data from the two other locations overlap with previous TiO_2 and P_2O_5 data from the CAVA. Sodium contents (expressed as Na_2O) vary between 1.8 and 5.1 wt%, and broadly increase with melt MgO content (Fig. 3B).

Lithium contents are between 3.2 and 20.2 ppm across the three volcanoes, with highest Li contents measured in Fuego glasses. Turrialba glasses are characterised by lower B contents (2.8-9.6 ppm) than Cerro Negro (8.9-20.2 ppm) and Fuego glasses (between 8.2-23.2 ppm for MIs only). Average B/Li ratios decrease from 2.3 at Cerro Negro to 1.4 at Fuego and finally to 0.7 at Turrialba. Lithium and B data for homogenised and unhomogenised inclusions overlap for both Fuego and Cerro Negro (Fig. 4A).

Volatile contents of the studied glasses are presented in Figs. 4B and 5. Turrialba inclusions are characterised by comparatively low H₂O (maximum 1.6 wt%) and high sulfur (maximum 3400 ppm) contents. Cerro Negro and Fuego inclusions have similar H₂O contents, between 3–5 wt% (Fig. 5A), close to the global arc MI average (Plank et al., 2013). Carbon contents of glasses expressed as CO₂, range from below detection limit (<80 ppm) up to 3410 ppm, with data from the three volcanoes overlapping. The highest CO₂ contents were measured in homogenised MIs, containing between 500 and 3400 ppm CO₂, while naturally-quenched glasses and MIs are mostly limited to a few 100 ppm CO₂ (Fig. 5). Lower CO₂ contents in naturally-quenched MIs are expected due to post-entrapment CO₂ loss to bubbles (e.g. MacLennan, 2017). The H₂O and S content of homogenised and unhomogenised MIs from Cerro Negro and Fuego overlap. The total S range in Cerro Negro, Fuego, and Turrialba glasses is 170–1810 ppm, 60–1560 ppm, and 205–3410 ppm, respectively. Uncorrected MI sulfur contents do not correlate with FeO; however, if only homogenised inclusions are considered, there is a broad positive correlation between FeO and S (Fig. 6A) for both our data and that published by Rasmussen et al. (2020).

Fluorine and chlorine contents of the studied glasses are between 250–2740 ppm and 290–3100 ppm, respectively (Fig. 4B). Turrialba glasses contain >2000 ppm F; higher than both Cerro Negro (240–540 ppm) and Fuego samples (440–960 ppm, excluding a single Fuego embayment with 1450 ppm F). Fuego MIs have higher Cl contents (>1300 ppm) than both Turrialba (770–1250 ppm) and Cerro Negro (290–1950 ppm) samples (Fig. 4B).

4.2. Sulfur speciation

Sulfur speciation ($S^{6+}/\Sigma S$) was measured on a subset of our glasses: seven from Cerro Negro (including three homogenised in-

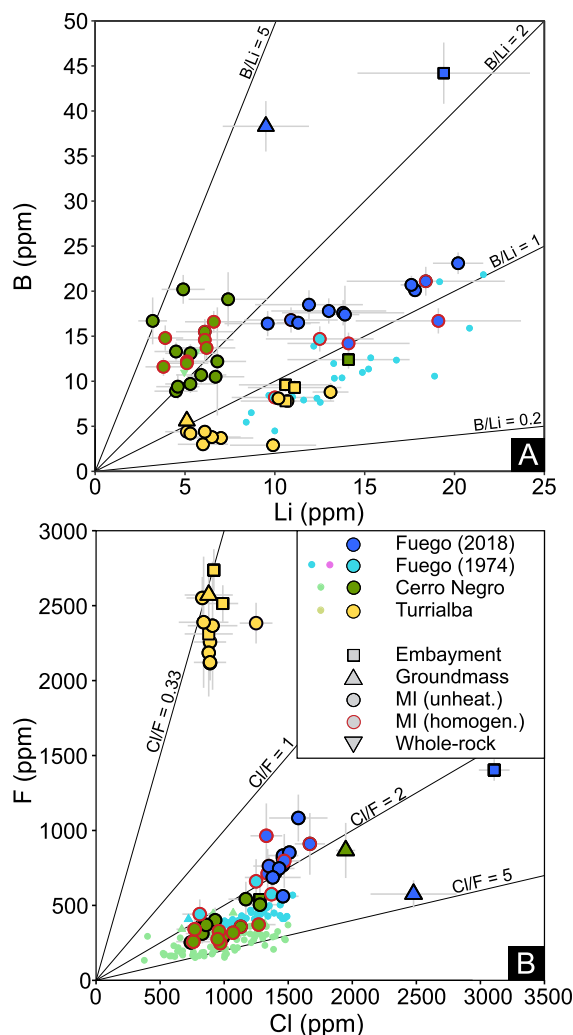


Fig. 4. (A) Boron versus lithium concentrations in the studied glasses. Literature data, shown as smaller circles without outlines, for Fuego (MIs) and Cerro Negro (whole-rocks) are from Lloyd et al. (2013) and Barth et al. (2019), respectively. (B) Halogen concentrations (F vs. Cl) in the studied glasses. Cl data collected by EPMA are plotted; F was only analysed using SIMS. A Fuego matrix glass and an embayment have considerably elevated Cl contents relative to our Fuego MI data (2500 and 3100 ppm, respectively). References to literature data are the same as in Fig. 3. Error bars are 2σ . In (B) we use Cl contents measured by EPMA rather than those measured by SIMS; the former has lower analytical uncertainty (see supplementary material).

clusions), five from Turrialba (four MIs, one embayment/matrix glass), and five from Fuego (Fig. 6B). After applying a correction to account for greater sulfate X-ray absorbance over sulfide (Nash et al., 2019), we find that natural Cerro Negro MIs have $S^{6+}/\Sigma S$ between 0.92 and 0.99. Turrialba glasses have $S^{6+}/\Sigma S$ between 0.95 and 1. Fuego glasses have $S^{6+}/\Sigma S$ between 0 and 0.75. For Fuego, low $S^{6+}/\Sigma S$ was measured in an embayment displaying matrix glass texture ($S^{6+}/\Sigma S=0.18$) and in a MI which potentially decrepitated and then re-sealed ($S^{6+}/\Sigma S=0$, see supplementary material for photos of samples). Three homogenised Cerro Negro inclusions have significantly lower $S^{6+}/\Sigma S$, between 0.03 and 0.08, than natural MIs. The cause of reduction in homogenised inclusions is currently under investigation and not discussed further in this work.

4.3. Sulfur isotopes in glasses

Sulfur isotope ratios presented here have been corrected for IMF (IMF varied between -5% and $+1\%$ in 2020 and -29% to $+3.7\%$ in 2022) using a linear S and $\ln(S)$ regressions for data

collected in 2020 and 2022, respectively (see supplementary material). Data collected from the same Fuego 2018 sample (but not the same MIs) during our 2020 and 2022 SIMS sessions fully overlap. Apart from a few sulfur-poor glass $\delta^{34}S$ analyses the IMF correction error, which is close to $\pm 1\%$ (1σ) for both 2019 and 2022, is the largest error for our data; this is reflected in the error bars of Fig. 7A. Correlation between glass S content and IMF was also observed by (Taracsák et al., 2021) using the same instrument and analytical procedures; in their dataset IMF varies between -12% and $+2\%$. Sulfur isotope ratios in Cerro Negro, Fuego and Turrialba glasses are between $+1.1\%$ to $+4.5\%$ ($n=19$), -0.5% to $+4.9\%$ ($n=19$), and 0% to 3.4% ($n=13$), respectively. Sulfur isotope ratios and sulfur concentrations weakly correlate (negatively) in Fuego glasses ($R^2=0.45$), but no significant correlation is observed for glasses from Cerro Negro ($R^2=0.29$) or Turrialba ($R^2=0.22$, Fig. 7). The three studied inclusions from the 1974 Fuego eruption have lower $\delta^{34}S$ values than the 2018 eruption glasses.

5. Discussion

5.1. The effects of MI homogenisation on volatile contents and sulfur isotopes

The volatile content of MIs may be altered by post-entrapment processes, linked to bubble formation (MacLennan, 2017), diffusion (e.g. Bucholz et al., 2013), sulfide precipitation (Danyushevsky et al., 2002), and formation of secondary mineral phases along phase boundaries (Schiavi et al., 2020). These processes may affect sulfur isotope ratios, S speciation, and S contents in MIs, masking the mantle signature.

To investigate the effect of post-entrapment processes on sulfur isotope ratios measured in CAVA MIs, we carried out re-homogenisation experiments on Fuego 2018 and Cerro Negro MIs at high pressure and temperature. Homogenising MIs at high partial H_2O pressure (using a hydrated matrix) and temperature has been shown to successfully dissolve bubbles within MIs, resulting in increased glass CO_2 contents without significant overheating and diffusive H-loss (Mironov et al., 2015; Rasmussen et al., 2020). We also analysed three re-homogenised inclusions from the 1974 eruption of Fuego, described in Rasmussen et al. (2020). We find elevated CO_2 contents in re-homogenised MIs from both Cerro Negro and Fuego compared to naturally-quenched inclusions (Fig. 5); these results are similar to Rasmussen et al. (2020) for Fuego 1974 and Segum 1977 MIs. The range of sulfur concentrations measured within re-homogenised and natural inclusions overlap (Figs. 5B, 6), indicating the bubbles contained little S in either gas or solid form. The sulfur content and the measured (uncorrected) total FeO content of homogenised MIs have a weak linear correlation ($R^2 = 0.33$, Fig. 6). Sulfide globules can be observed in reflected light photographs (see supplementary images) within two re-homogenised Fuego MIs. S speciation data indicate that most sulfur stored within the glass phase has been reduced during experiments. For Cerro Negro samples, $S^{6+}/\Sigma S$ ratio decreases from ~ 1 in natural MIs to ~ 0 in homogenised MIs. The sulfur isotopic composition of re-homogenised MIs from Cerro Negro ($2.9 \pm 1.0\%$, $n=8$, 1σ) and Fuego 2018 ($2.4 \pm 0.9\%$, $n=4$) overlap with average values measured in natural inclusions ($3.0 \pm 0.8\%$, $n=11$ for Cerro Negro; $3.3 \pm 1.1\%$, $n=12$ for Fuego; Fig. 7), indicating that post-entrapment processes or the re-homogenisation experiments do not significantly change the sulfur budget and isotopic composition of CAVA MIs. Three re-homogenised MIs from the 1974 eruption of Fuego have comparatively negative $\delta^{34}S$ (-0.5% to 0.0%) compared to both naturally quenched and re-homogenised Fuego 2018 MIs; these few data may suggest that the two eruptions were fed by magmas with different S isotope compositions. Nonetheless, more data are needed for in-depth comparison.

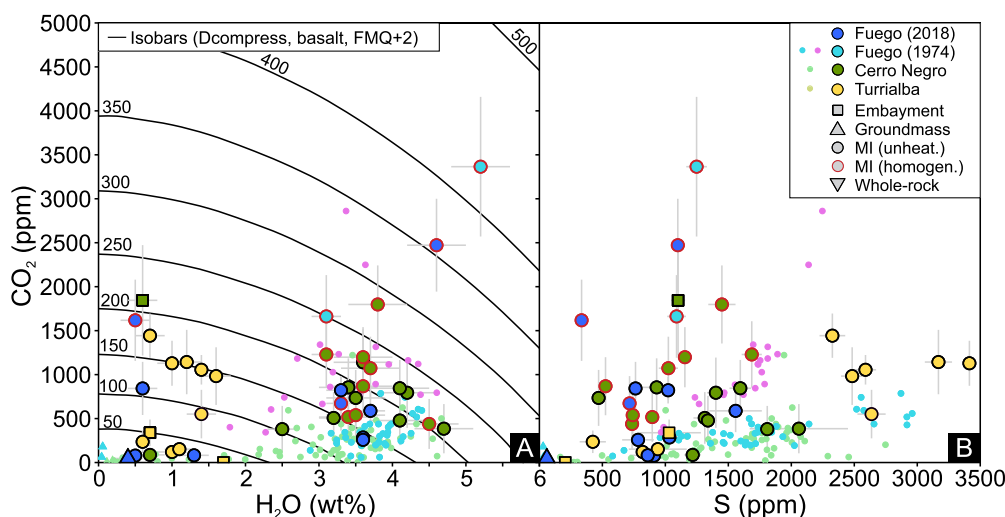


Fig. 5. Volatile contents in the studied glasses, plotted as CO_2 vs. H_2O (A) and CO_2 vs. S (B). Solid black lines in (A) are isobars calculated using DCompress (Burgisser et al., 2015), using the default basaltic composition of the software at an $f\text{O}_2$ value of FMQ+2 and a temperature of 1150 °C. Numbers next to the isobars are pressure expressed as MPa. Symbols and references for literature data are the same as in Fig. 3. Error bars are 2σ . In (B) we use S contents analysed by SIMS due to the lower analytical error compared to EPMA data. Generally, S contents measured by SIMS and EPMA show good agreement (see supplementary material). Literature data shown as smaller circles without outlines are from the same sources as those plotted in Figs. 3 and 4 (Lloyd et al., 2013; de Moor et al., 2016; Barth et al., 2019; Rasmussen et al., 2020) and follows the same symbol colouring scheme.

5.2. Sulfur degassing of CAVA magmas

Sulfur solubility in melts decreases with decreasing pressure, leading to sulfur degassing and sulfur isotope fractionation (Sakai et al., 1982; de Hoog et al., 2001). Heavier sulfur isotopes preferentially partition into more oxidised phases (such as sulfates) making the sulfur isotope gas-melt fractionation factor ($\alpha_{\text{gas-melt}}$) a redox dependent parameter (e.g. Marini et al., 2011).

During magma degassing, the exsolved fluid phase is buoyant and may separate from the melt effectively, depending on bubble size and melt rheology. Sulfur degassing may therefore be approximated as occurring in either open- (likely prevailing at low pressure) or closed-system conditions (e.g. Edmonds et al., 2022).

In Fig. 7 we quantify average $\alpha_{\text{gas-melt}}$ and average initial $\delta^{34}\text{S}$ composition of CAVA melts by fitting a regression between the natural logarithm of the fraction of remaining sulfur present in the melt ($\ln(S_{\text{melt}}/S_{\text{max}})$) and the natural logarithm of the measured sulfur isotope ratios. This assumes pure open system degassing. A regression between $\ln(S_{\text{melt}}/S_{\text{max}})$ and $^{34}\text{S}/^{32}\text{S}_{\text{melt}}$ is calculated for each of the three studied volcanoes using an error-in-variables, total least squares regression approach (Deming regression, e.g. Ripley and Thompson, 1987, Fig. 7A). From these regressions, we determine the average undegassed melt $\delta^{34}\text{S}$ and $\alpha_{\text{gas-melt}}$ for each volcano; the former is calculated from the intercept, while the latter is derived from the slope of the regressions. Errors for these two parameters are estimated by propagating the standard error (S.E.) of the intercept and the slope calculated for each regression fit. It is possible to perform similar, regression-based modelling assuming a closed system. However, errors associated with closed system models are more than double those of the open system approach, hence we favour the latter. In reality, degassing-related isotope fractionation may be best described by a mixture of these two end-member processes (see supplementary material for further detail).

Using the regression based-method (Fig. 7), we estimate an average $\alpha_{\text{gas-melt}}$ of 0.999 ± 0.0018 and 0.999 ± 0.0014 (2 S.E.) for Cerro Negro and Fuego, respectively. A $\alpha_{\text{gas-melt}}$ of 1.000 ± 0.0014 is derived for Turrialba (see supplementary material for further discussion). These values indicate that isotope fractionation during sulfur degassing is limited, with permil-level changes only expected after degassing has removed between 60 to 80% of sul-

fur from the melt. These fractionation factors comparable to those estimated for basaltic andesites from Anatahan volcano in the Marianas (0.9983–0.9993, de Moor et al. (2010)) and for Indonesian basalts and basaltic andesites (0.9996–1.0004, de Hoog et al. (2001)).

Using the calculated average $\alpha_{\text{gas-melt}}$ values and undegassed melt S isotope estimates presented in Fig. 7 the sulfur isotope composition of the gas phase can be calculated (Sakai et al., 1982). At the initial phase of S degassing ($S_{\text{melt}} > 1000$ ppm), $\delta^{34}\text{S}_{\text{gas}}$ is estimated at -2‰ to 1‰ for Fuego, increasing to $+1\text{‰}$ and $+3\text{‰}$ for Cerro Negro and Turrialba (Fig. 7C). A larger range in $\delta^{34}\text{S}$ is expected during later, shallow degassing, with the gas composition reaching $+8\text{‰}$ at Fuego and Cerro Negro during the final degassing stage. Turrialba gases are expected to have nearly constant $\delta^{34}\text{S}$ (between 0‰ and $+3\text{‰}$) due to the small fractionation factor estimate (Fig. 7C).

Direct comparison of modelled and measured $\delta^{34}\text{S}_{\text{gas}}$ values can be made (Fig. 7B,C) at Cerro Negro (de Moor et al., 2022). At Turrialba, comparison is possible between melts that fed the 1865 eruption and gas from the 2014 eruption; we note the latter eruption was fed by melts with more evolved composition (de Moor et al., 2016). Low temperature gases at Cerro Negro have $\delta^{34}\text{S}$ values between $+2\text{‰}$ and $+5\text{‰}$, which overlaps with our estimate for Cerro Negro gas compositions (Fig. 7B,C). We note that sulfur isotope ratios measured in low temperature Cerro Negro gases may have been affected by hydrothermal processes to some extent (de Moor et al., 2022). Hot ($>450^\circ\text{C}$) Turrialba gases have a $\delta^{34}\text{S}$ range of 0‰ to $+4\text{‰}$, with an average composition of $+3\text{‰}$; our gas composition estimates match this range. Overall, we find relatively good agreement between our modelled $\delta^{34}\text{S}$ values and the data of de Moor et al. (2022). We conclude that glass S- $\delta^{34}\text{S}$ trends accurately record degassing processes, which can be backtracked to derive the isotopic composition of undegassed, mantle-derived melts.

5.3. Slab-derived sulfur in arc magmas and the mantle wedge

Arc magmas are partial melts of a mantle wedge that has been metasomatised by slab-derived components rich in highly fluid mobile elements (e.g. B and Cl, Fig. 4). However, whether the slab-derived components also deliver excess sulfur (Lee et al., 2018;

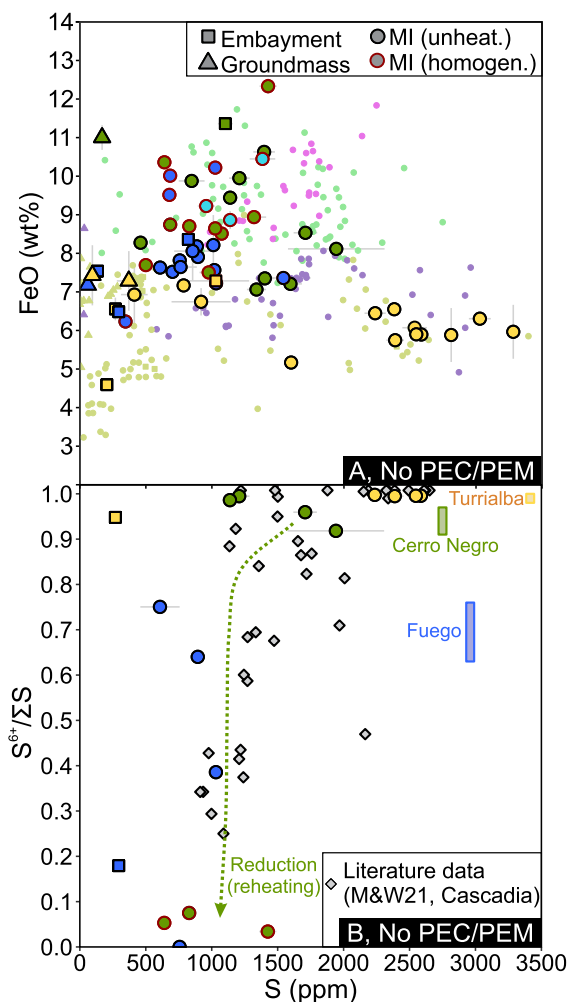


Fig. 6. (A) Composition of studied glasses FeO (total) vs. S diagram. References to the literature data (smaller circles without outlines) are the same as in Fig. 3. Data presented here are analysed glass compositions (uncorrected for post-entrapment crystallisation/melting and diffusive Fe-loss), as we intend to demonstrate potential relationship between FeO and S in response to sulfide formation, the effect of which may get overprinted by the PEM/PEC and diffusive Fe-loss correction procedures. (B) Sulfur speciation of CAVA glasses vs. S content. Grey diamonds are primitive MI literature data from Southern Cascadia (Muth and Wallace, 2021). Rectangles show expected primary melt S content and S speciation, based on maximum MI S content and the S speciation of the two most S-rich MI presented here. Error bars represent 2σ uncertainty.

Muth and Wallace, 2021); whether the slab component delivers sulfur in an oxidised or reduced form (Jégo and Dasgupta, 2014; Piccoli et al., 2019; Walters et al., 2020); and which part of the slab it may originate from (Muth and Wallace, 2021; de Moor et al., 2022; Kawaguchi et al., 2022) remain unclear.

Sulfur isotope ratios of primary arc magmas can be used to infer the origin of sulfur in the mantle wedge (Gurenko, 2021; Muth and Wallace, 2021; de Moor et al., 2022; Kawaguchi et al., 2022), as various slab components have distinct isotopic composition compared to DMM (Alt and Shanks, 2003; Alt et al., 2012; Labidi et al., 2012; de Moor et al., 2022). In Fig. 7 we present quantitative, regression-based estimates for primary, undegassed melt sulfur isotope ratios from the three studied volcanoes. Maximum measured MI sulfur contents are 2748 ppm, 2959 ppm, and 3414 ppm for Cerro Negro, Fuego and Turrialba, respectively. Modelled average primary melt $\delta^{34}S$ values are $+0.7 \pm 1.4\text{‰}$ for Fuego, $+1.6 \pm 0.8\text{‰}$ for Turrialba, and $+2.2 \pm 1.0\text{‰}$ for Cerro Negro (2 S.E.). The three average primary melt $\delta^{34}S$ are therefore within error, and show no relationship to Ba/La (Fig. 8C), the slab tracer that

varies so systematically along strike at the CAVA (Fig. 1B). Our primary melt $\delta^{34}S$ estimates for Cerro Negro and Turrialba are $\sim 2\text{‰}$ lower than those calculated from the gas data by de Moor et al. (2022) for the same volcanoes (Fig. 8). This difference can be explained if gas samples contained larger fraction of sulfur degassed at shallower depth, which can be slightly heavier than S degassed at greater depth (Fig. 7).

Sulfur isotope ratios alongside fO_2 estimates are also available from the Cascades (Lassen volcanic complex, Muth and Wallace (2021)). Lassen MIs underwent negligible S degassing (Muth and Wallace, 2021), hence a direct comparison with CAVA primary melt estimates can be made (Fig. 8A). Lassen magmas have larger $\delta^{34}S$ variation (1‰ to $+5.5\text{‰}$) than our primary melt estimates for CAVA volcanoes ($+1\text{‰}$ to $+2\text{‰}$, Fig. 8). Although the fO_2 of CAVA melts is comparable to some of the more oxidised Lassen magmas, primary melt $\delta^{34}S$ values at given fO_2 are up to 4‰ higher at Lassen than at the CAVA (Fig. 8B).

Further comparisons can be made between CAVA, Cascades (Muth and Wallace, 2021), and Kyushu (Kawaguchi et al., 2022) MI sulfur isotope data and trace element ratios sensitive to slab-wedge interaction, such as Sr/Nd, Ba/La, and Pb/Ce (Fig. 8). The relationship between $\delta^{34}S$ and Sr/Nd is complicated: for Lassen, $\delta^{34}S$ and Sr/Nd correlate positively, for Kyushu this correlation is negative for a subset of samples with $\delta^{34}S$ above $+3\text{‰}$, while for the CAVA there is no correlation. While $\delta^{34}S$ broadly increases with Pb/Ce for all three arcs, at given Pb/Ce the variability in $\delta^{34}S$ is between 5 to 7‰ (Fig. 8D). Global comparison of arc melt $\delta^{34}S$ datasets show that sulfur isotopes may correlate differently, or not at all, with trace element ratios indicative of slab-mantle interaction, such as Sr/Nd and Ba/La, or fO_2 (Fig. 8). Therefore, the $\delta^{34}S$ of arc melts is not a simple proxy for arc magma fO_2 or slab-wedge interaction.

Compared to MORBs, which have an average $\delta^{34}S$ of $-0.9 \pm 0.5\text{‰}$ (Labidi et al., 2012), all three CAVA volcanoes have elevated average initial $\delta^{34}S$ values (Fig. 7A), consistent with all other arc $\delta^{34}S$ measurements, including gases, MIs, and whole rock samples. This may be explained if a slab-derived component is able to elevate mantle wedge and primary arc melt $\delta^{34}S$ (Alt et al., 2012; de Moor et al., 2022) and consequently S contents. Crustal processing may also explain elevated $\delta^{34}S$ and S contents in CAVA magmas if sulfide and/or sulfate with relatively high $\delta^{34}S$ is assimilated during magma storage (Chowdhury and Dasgupta, 2019). However, extensive assimilation is unlikely to have affected any of the three studied locations: Cerro Negro and Turrialba samples are comparatively primitive, containing olivines with >80 mol% forsterite (Fig. 2A). Furthermore, Fuego, Cerro Negro, and Turrialba magmas have Sr-Nd isotope systematics consistent with an upper mantle source ($^{87}S/^{86}Sr$ between 0.7036–0.7039 and $^{143}Nd/^{144}Nd$ between 0.51295–0.51311, Feigenson and Carr, 1986; Plank, 2005; Hoernle et al., 2008; Heydolph et al., 2012; Di Piazza et al., 2015) and suggest minimal crustal assimilation. The lack of evidence for crustal assimilation at these locations points to slab-derived sulfur as the cause of elevated $\delta^{34}S$, S content, and fO_2 in CAVA arc magmas.

5.4. The sulfur content of the mantle wedge and the sulfur isotopic composition of slab fluids

Previous work to constrain the behaviour of sulfur and other redox sensitive elements in subduction zones mainly focused on fluxes of S between the slab, mantle wedge, and arc volcanoes (de Moor et al., 2022), the redox and oxygen budget of subduction zones (e.g. Evans, 2012; Stolper et al., 2021), or the relationship between melt S content and other volatiles and trace elements (Muth and Wallace, 2022). However, in depth investigation of mantle wedge sulfur concentrations across volcanic arcs is rare: prior estimates include 500 ppm for the Luzon arc (Métrich et al., 1999), 300–450 ppm based on a global arc dataset (Zhao et al., 2022), and

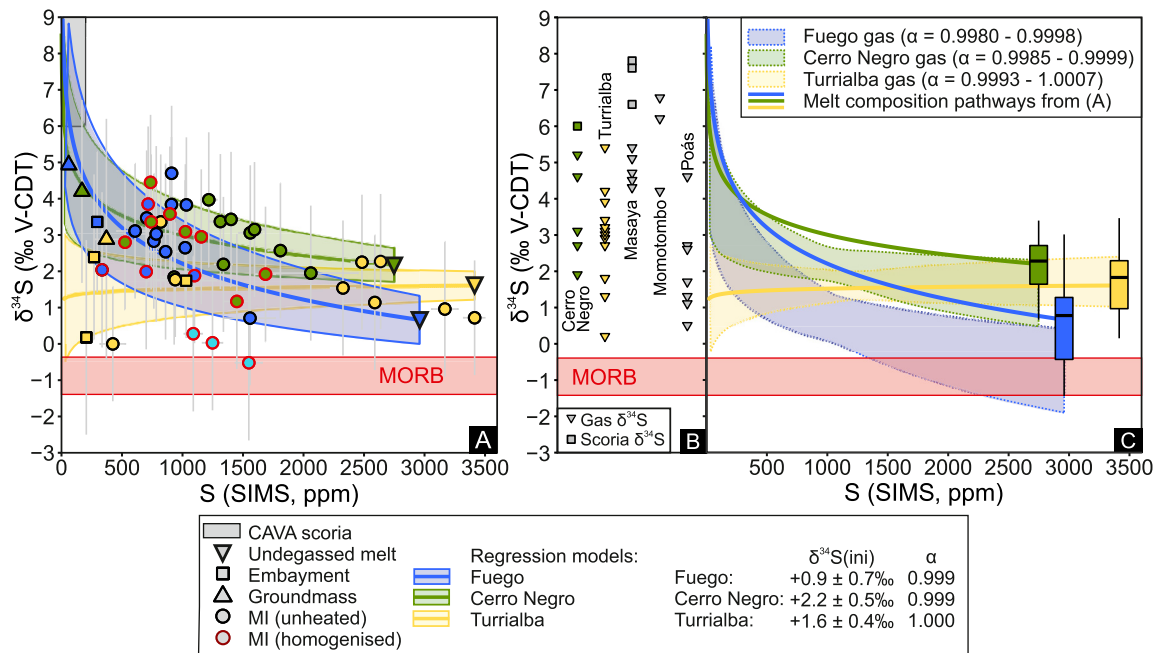


Fig. 7. (A) IMF-corrected sulfur isotopic composition of studied melt inclusions plotted against sulfur content (measured by SIMS). Symbol colours are the same as for previous figures. Solid lines are open system Rayleigh fractionation curves calculated using a regression between $\ln(\text{S})$ and $\ln(\delta^{34}\text{S})$. Shaded areas represent the regression uncertainty and are calculated using the standard error of each regression. Downward-pointing triangles indicate the parental, undegassed melt $\delta^{34}\text{S}$ for each volcano, calculated from the extension of the regressions. These values are within uncertainty of those measured in MIs with the highest S concentration. Grey area in (A) represent the range of CAVA scoria $\delta^{34}\text{S}$ compositions (data from de Moor et al. (2022)), assuming scoria S contents of <250 ppm. (B) Gas (downward triangle) and scoria (square) data for CAVA volcanoes, taken from de Moor et al. (2022). (C) Modelled gas compositions for each volcano (shaded areas) as a function of melt S content. Gas $\delta^{34}\text{S}$ composition is calculated using the method of Sakai et al. (1982). The shaded area represents the range of possible gas compositions if the errors of the modelled, undegassed melt S isotope estimates and $\alpha_{\text{gas-melt}}$ values are considered. The box and whiskers plots in (C) represent the estimated, undegassed S isotope compositions for each of our glass analyses, and were calculated using the regression-based fractionation factors assuming original melt S contents were equal to the highest S content measured in each volcano, using data from this work and Lloyd et al. (2013); Barth et al. (2019). Pink field is based on the MORB dataset of Labidi et al. (2012). Error bars in (A) are 2σ and represent the largest of these three errors: internal precision (standard error of the counting cycles of each analyses by the CAMECA CIPS software), external precision (defined as the standard deviation of the primary standard measured in each session), or IMF calibration error (the standard residual error of the regression used to calculate IMF at given S content). Errors of the average $\delta^{34}\text{S}_{\text{ini}}$ quoted in the caption are 1 S.E. calculated from the regression intercept and slope standard errors.

200–500 ppm used by Chowdhury and Dasgupta (2019) for modelling.

We use mass balance modelling to quantitatively estimate the S content of the mantle wedge under the CAVA. We follow the modelling steps described by Kelley et al. (2006) to estimate mantle melting degrees under volcanic arcs. As a first step, we selected whole rock compositions that contain more than 5 wt% MgO from each studied volcano (Plank, 2005; Reagan et al., 2006; Di Piazza et al., 2015; Barth et al., 2019). Whole-rock compositions were corrected for crystallisation by adding increments of olivine until the composition of each sample reached equilibrium with Fo₉₁ olivine. Central American magmas potentially crystallise clinopyroxene and plagioclase before reaching 5 wt% MgO: this leads to uncertainties in Ca, Fe, Mg and Si contents for our corrected whole-rock compositions (Sadofsky et al., 2008). However, elements incompatible in pyroxene, olivine, and anorthitic plagioclase, such as Ti, Na, and Zr, should remain reliable indicators of melting degree. Filtering at a higher MgO content is hindered by the relatively low MgO (<7 wt%) content of Turrialba whole-rock samples (Reagan et al., 2006; Di Piazza et al., 2015). The main source of error in our model is the olivine-melt Mg-Fe partition coefficient: we use a value of 0.3 ± 0.03 (Putirka, 2008). While the Ti content of Turrialba whole rock samples used for the modelling are lower than those measured in our MIs, whole-rocks are more Mg-rich (Fig. 3) and likely better represent the mantle source of Turrialba melts. Samples used for the calculations cover much of the Holocene eruptive history of Turrialba (Reagan et al., 2006).

Melting models were run using multiple mineralogies and starting compositions, including garnet and spinel lherzolite, DMM and primitive mantle (PM, Fig. 9A,B). We find that, regardless of us-

ing Ti, Na, or Zr, melting degree increases in the following order: Turrialba < Fuego < Cerro Negro. This agrees with Sadofsky et al. (2008) who also found the highest melting degrees under Nicaragua, and is also consistent with the inverse relationship between melting degree and crustal thickness demonstrated by Turner et al. (2015), given that the crust under Nicaragua is thinner than under Guatemala and Costa Rica. We utilise $\text{Ti}_{(\text{Fo}91)}$ as a proxy for melting degree (Kelley et al., 2006; Sadofsky et al., 2008), assuming a DMM spinel lherzolite source and equilibrium melting. Using $\text{Ti}_{(\text{Fo}91)}$ a melting degree of $7 \pm 2.5\%$ is estimated for Turrialba, which increases to $12 \pm 1\%$ at Fuego and $17 \pm 0.4\%$ at Cerro Negro (1σ).

Using these estimates, alongside undegassed melt S content estimates, we modelled the S content of the mantle wedge, assuming perfect incompatible behaviour for S ($S_{\text{mantle}} = S_{\text{melt, max}}/F$). To estimate uncertainties, we carried out Monte Carlo simulations (Fig. 10A). Models were calculated by randomly sampling input values 100000 times: these include melting degree, DMM S content (150 ± 50 ppm Ding and Dasgupta (2017)), primary melt $\delta^{34}\text{S}$ (from Fig. 7), and slab component S content (5 ± 1 wt%, based on experiment G246 in Jégo and Dasgupta (2014); minimum slab component S content was set at 950 ppm based on anhydrite saturation (Zajacz and Tsay, 2019) in a rhyolitic/dacitic melt like experiment G246). No error was assumed for undegassed melt S contents, as this cannot be quantified meaningfully due to the contrasting effects of degassing (decreases S) and silicate crystallisation (increases S). For Turrialba, we estimate a mantle wedge S content of 242 ± 85 ppm, increasing to 355 ± 30 ppm at Fuego and 462 ± 11 ppm at Cerro Negro (1σ , Fig. 10A). While the low end of the mantle S contents for Turrialba overlap with DMM (150 ± 50

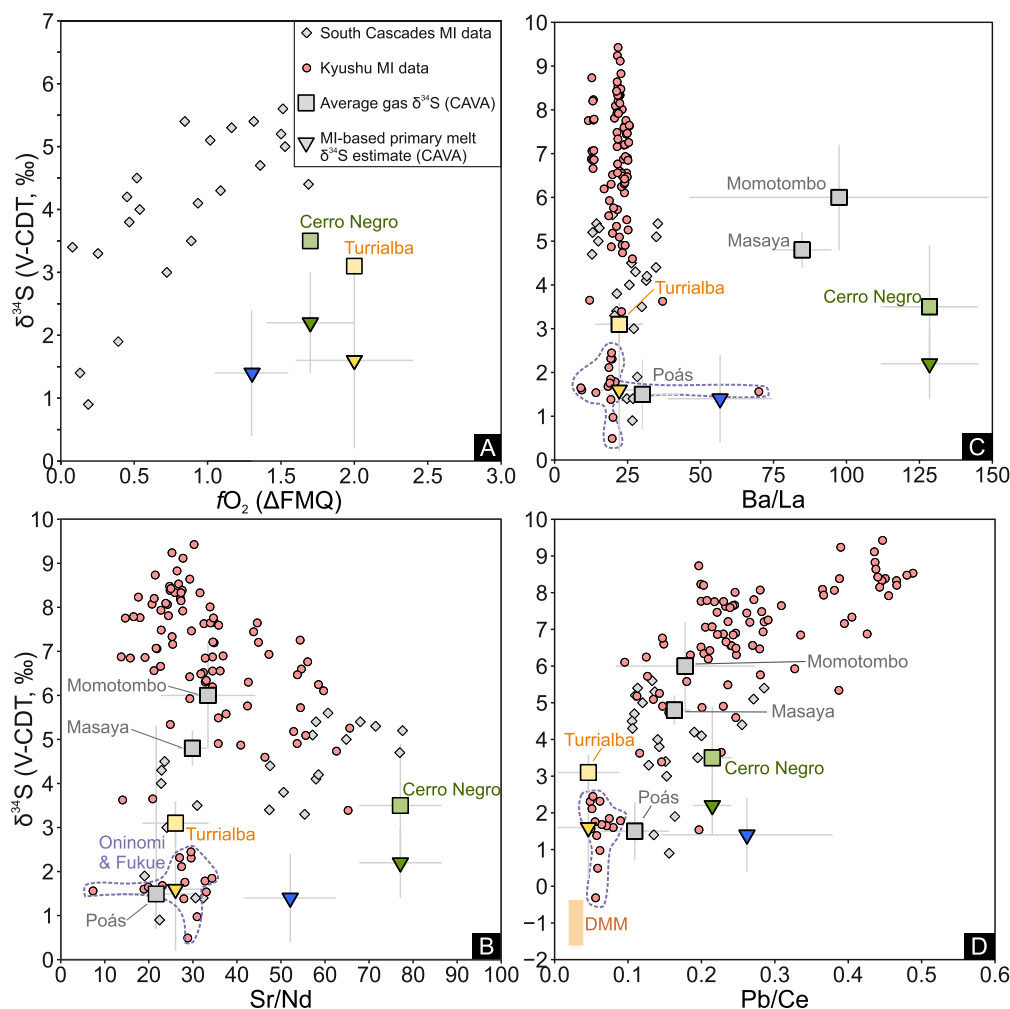


Fig. 8. (A) Comparison of gas-based (squares, de Moor et al., 2022) and MI-based (downward triangles, see previous figures for colour scheme) primary melt sulfur isotope ratio estimates at the CAVA on a $\delta^{34}\text{S}$ vs. $f\text{O}_2$ diagram (A). Colour squares represent melt $\delta^{34}\text{S}$ estimates derived from gas data for Cerro Negro and Turrialba (de Moor et al., 2022). Oxygen fugacity estimates for Fuego (only considering data from Fo_{77-78} olivines) and Cerro Negro ($\text{Fo} > 80$ olivines) are based on olivine-melt V partitioning data (Lloyd et al., 2013; Barth et al., 2019), while Turrialba $f\text{O}_2$ is based on olivine-spinel oxybarometry (supplementary material). Oxygen fugacity (based on $\text{Fe}^{3+}/\Sigma\text{Fe}$) and $\delta^{34}\text{S}$ measured in MIs for the Cascades (Muth and Wallace, 2021) is also shown in (A). Inter-arc comparison of Cascades (Muth and Wallace, 2021), Kyushu (Kawaguchi et al., 2022) and CAVA magmas on $\delta^{34}\text{S}$ vs. Sr/Nd (B), Ba/La (C), and Pb/Ce (D) diagrams. Fuego, Cerro Negro and Turrialba trace element compositions are based on MgO-rich (>5 wt%) whole rock samples, including Fuego (Plank, 2005), Cerro Negro (Barth et al., 2019) and Turrialba (Reagan et al., 2006; Di Piazza et al., 2015). The Pb/Ce ratio of the DMM is from Salters and Stracke (2004), while $\delta^{34}\text{S}$ is from Labidi et al. (2012). Purple dashed line indicates high-Nb Kyushu samples from Fukue and Oninome; notably, these data points overlap with data from Costa Rica (Turrialba, Poás), locations that are known to erupt Nb-rich magmas (Reagan and Gill, 1989; DeVitre et al., 2019). Grey squares in (B-D) are locations from the CAVA with only gas data available (de Moor et al., 2022).

ppm, Ding and Dasgupta (2017)), values for Fuego and Cerro Negro are clearly higher. Based on our mantle wedge S content estimates and on a DMM S content of 150 ± 50 ppm (Ding and Dasgupta, 2017), we calculate that $\sim 70\%$ of S present in the melting mantle wedge under Nicaragua originates from the slab. At Turrialba the contribution of the slab-derived component to the mantle wedge sulfur budget decreases to 20–60%. However, this value is uncertain as melting degree estimates at Turrialba have a >30% relative error. Mantle flow delivering more enriched material to the mantle wedge under Costa Rica (Herrstrom et al., 1995) or the subduction of oceanic crust with OIB provenance (Benjamin et al., 2007; Hoernle et al., 2008; Gazel et al., 2009) could influence the Na, Ti, and Zr contents of mantle under Turrialba. To explore how an enriched mantle source may influence our model results we carried out calculations assuming a PM mantle wedge composition alongside our DMM model (Fig. 10). Using a PM composition, melting degree under Turrialba increases to $16 \pm 4\%$ (using Ti contents, Fig. 9A). This increase in melting degree drives our mantle wedge S content estimate to 540 ± 140 ppm at Turrialba. The proportion of

slab-derived S is $53 \pm 15\%$, overlapping with the DMM-based model estimate (Fig. 10).

Treating sulfur as a perfectly incompatible element is only correct if total S loss from sulfur bearing phases is achieved (Lee et al., 2012). If this is not the case, then any estimate calculated assuming perfect incompatibility will yield a minimum. To investigate whether total sulfur removal in the mantle wedge under the CAVA is feasible, we modelled the S solubility of Fuego, Cerro Negro, and Turrialba primary melts (Fig. 9D). Using the sulfur concentration at anhydrite saturation (SCAS) model of Zajacz and Tsay (2019) at 1300°C and the model of Fortin et al. (2015) to estimate the sulfur concentration at sulfide saturation (SCSS) at 1300°C and 2 GPa we directly calculate S solubility for CAVA magmas under mantle wedge conditions using measured $\text{S}^{6+}/\Sigma\text{S}$ values from MIs and utilising the model of Jugo et al. (2010). We also estimated S solubility for mantle wedge melts by converting independently constrained $f\text{O}_2$ (vanadium partitioning data from Lloyd et al. (2013); Barth et al. (2019) or spinel-olivine oxybarometry from this work) first to $\text{Fe}^{3+}/\Sigma\text{Fe}$ using the model of O'Neill et al. (2018) then converting

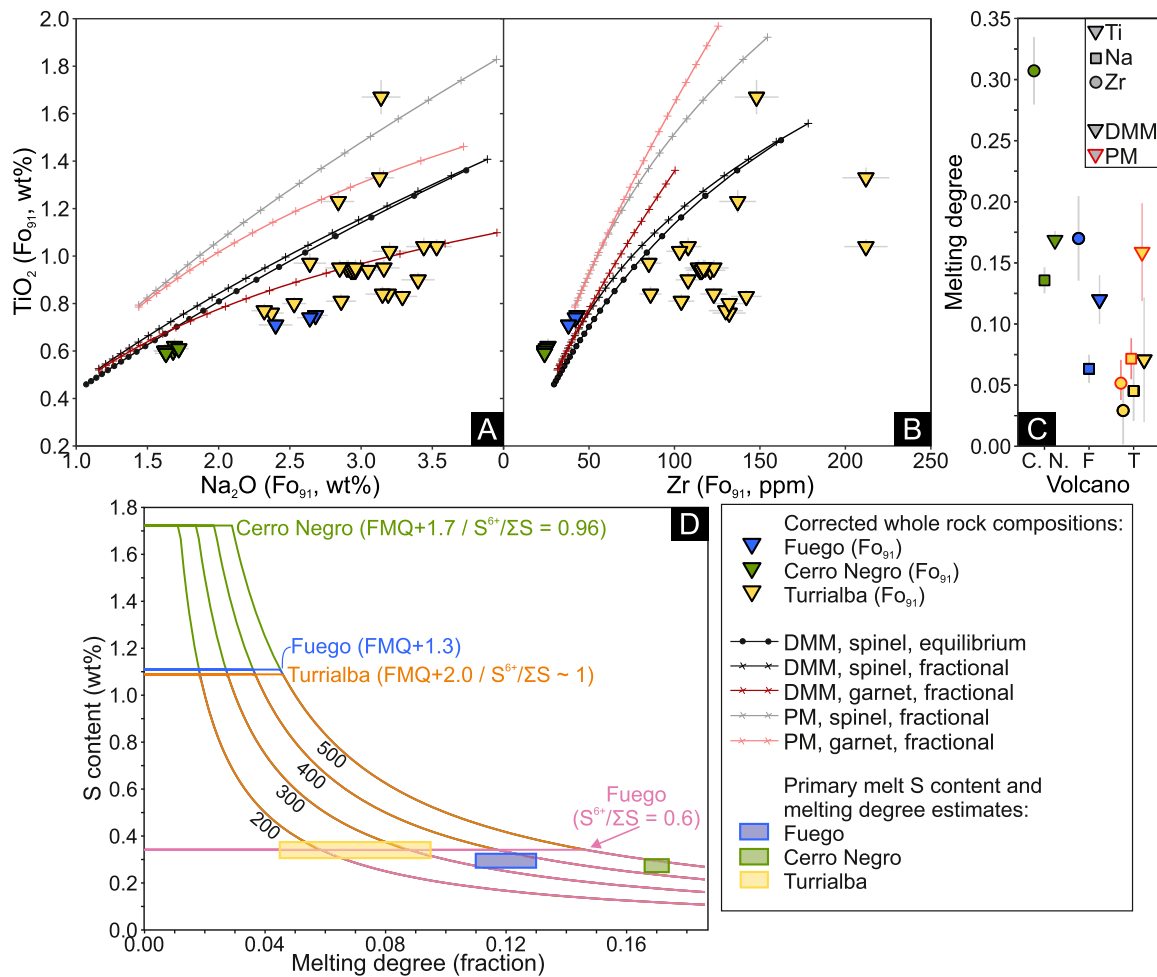


Fig. 9. Estimated melting degrees for fractionation-corrected CAVA whole-rock samples on $\text{TiO}_2(\text{Fo}_{91})$ vs. $\text{Na}_2\text{O}(\text{Fo}_{91})$ (A) and $\text{Zr}(\text{Fo}_{91})$ (B) diagrams. The four melting curves with crosses and the single curve with circles are calculated using accumulated fractional melting and equilibrium melting, respectively (modelling parameters are reported in the supplementary spreadsheets). Crosses and circles indicate 1% melting steps. In (C), melting degree calculated for each location using either Ti (downwards triangle), Na (square) or Zr (circle), assuming a DMM (black outline) and PM (red outline) spinel lherzolite source and equilibrium melting. A PM source was only applied to Turrialba, as this is the only location in our study where a significantly enriched mantle source can be justified. (D) Modelled S contents of mantle-derived melt as a function of melting degree at variable $f\text{O}_2$ or $\text{S}^{6+}/\Sigma\text{S}$ and mantle S content (the latter varies from 200 ppm to 500 ppm). Sulfur solubilities are calculated using composition-dependent SCSS/SCAS (Fortin et al., 2015; Zajacz and Tsay, 2019) values combined with either measured $\text{S}^{6+}/\Sigma\text{S}$ values (i.e. pink lines for Fuego) from our most S-rich MIs or calculated $\text{S}^{6+}/\Sigma\text{S}$ based on independent $f\text{O}_2$ estimates available at each of the studied volcanoes (i.e. blue lines for Fuego). Modelled $\text{S}^{6+}/\Sigma\text{S}$ values are derived by first converting $f\text{O}_2$ to $\text{Fe}^{3+}/\Sigma\text{Fe}$ using the empirical model of O'Neill et al. (2018) then converting $\text{Fe}^{3+}/\Sigma\text{Fe}$ to $\text{S}^{6+}/\Sigma\text{S}$ using the T-dependent model of Nash et al. (2019) at 1300 °C. Measured and modelled $\text{S}^{6+}/\Sigma\text{S}$ are close to identical at Turrialba (orange lines) and Cerro Negro (green lines); therefore, only a single set of melting curves are calculated for these locations. Boxes represent primary melt S estimates alongside the $\text{Ti}_{(\text{Fo}_{91})}$ -based melting degree estimates. While Turrialba melts are more oxidised (FMQ+2) than Fuego (FMQ+1.3), due to the composition dependence of the SCAS (Zajacz and Tsay, 2019) Fuego primary melts are modelled to be slightly more S-rich using independent $f\text{O}_2$ estimates.

those values to $\text{S}^{6+}/\Sigma\text{S}$ using the model of Nash et al. (2019) at 1300 °C (see supplementary material).

Using the measured $\text{S}^{6+}/\Sigma\text{S}$ values, S solubility at Fuego, Turrialba, and Cerro Negro is estimated at 0.35 wt%, 1.1 wt%, and 1.7 wt%, respectively (Fig. 9D). Converting independent $f\text{O}_2$ to $\text{S}^{6+}/\Sigma\text{S}$ results in an S solubility estimate of 1.1 wt% at Fuego; at Cerro Negro and Turrialba the two estimates are indistinguishable. At Cerro Negro and Turrialba sulfur solubility in the mantle wedge is higher than primary melt S contents (0.27 and 0.34 wt%, Fig. 7): here primary melts will be sulfur undersaturated and complete sulfide removal from the wedge is expected. At Fuego, total sulfide removal is less likely if redox conditions are slightly more reducing than those determined using the most primitive olivines (FMQ+1.3 Lloyd et al. (2013)). This means that we can only give a confident estimate for the lower bound of mantle S contents at Fuego, which is ~300 ppm (Fig. 9D).

We further test whether sulfide exhaustion under the CAVA is realistic using fractionation-corrected Cu contents and Cu/Zr ratios measured in primitive ($\text{MgO} > 6$ wt%) CAVA whole-rock samples

alongside the modelling procedures of Zhao et al. (2022) (see supplementary material). At Cerro Negro total sulfide removal from the source is confirmed by melt $\text{Cu}_{(\text{Fo}_{91})}$ contents and Cu/Zr ratios. At Turrialba and Fuego $\text{Cu}_{(\text{Fo}_{91})}$ contents and Cu/Zr ratios do not indicate total sulfide exhaustion from the mantle wedge. The copper content of Fuego melts may be achieved at an $f\text{O}_2$ of FMQ+1 to FMQ+1.3 of the mantle wedge contained no more than 500 ppm S: we propose this is the upper bound of mantle S content at Fuego. Copper contents are likely to be a less reliable indicators of sulfide exhaustion at Turrialba compared to independent $f\text{O}_2$ estimates due to the OIB-provenance of the magmas, which complicates trace element melting modelling. Therefore, at Turrialba we prefer the results of the sulfur content-based melting model rather than the Cu/Zr ratios-based approach; the former suggests total sulfur loss from the source.

Using our data alongside literature estimates of DMM S content (150 ± 50 ppm, Ding and Dasgupta (2017)) and $\delta^{34}\text{S}$ ($-0.9 \pm 0.5\%$ Labidi et al. (2012)) allows us to determine the $\delta^{34}\text{S}$ of the slab component. Results of the modelling are presented in Fig. 10C.

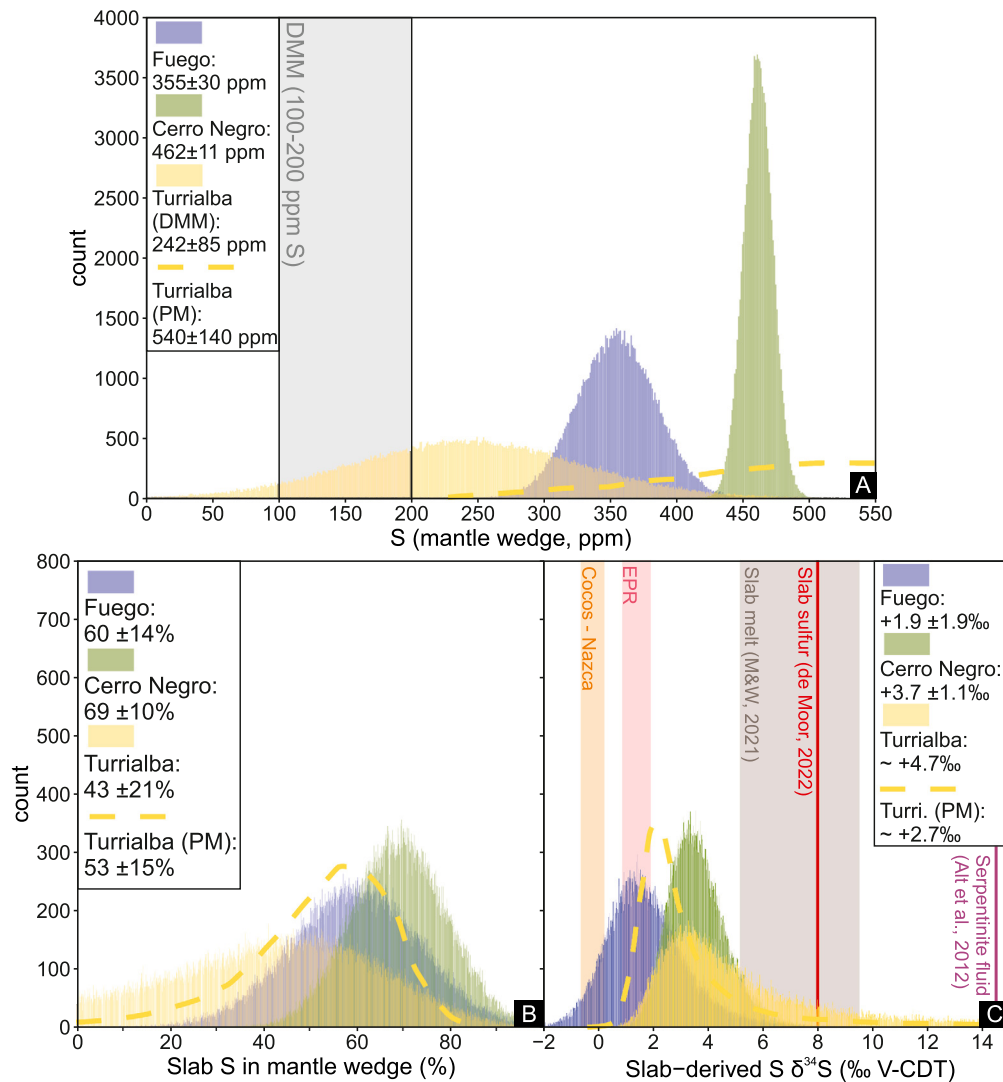


Fig. 10. Results of Monte Carlo simulations on histograms, showing modelled S contents (A) and the proportion of slab-derived S in the mantle wedge (B) alongside the isotopic composition of slab-derived S (C). Red and orange bars in (C) are subduction input estimates for the East Pacific Rise (EPR) and the Cocos-Nazca Ridge (de Moor et al., 2022). The brown bar in (C) is the composition of slab melt proposed by Muth and Wallace (2021) for Cascadia. The red line is the $\delta^{34}\text{S}$ of the slab component under the CAVA (de Moor et al., 2022), while the purple line is a serpentinite-derived fluid composition (Alt et al., 2012) estimated from ophiolite data. The thick, dashed yellow line show the outline of a Monte Carlo simulation for Turrialba using a PM composition, using an 200–300 ppm S content and a slightly enriched (chondritic) $\delta^{34}\text{S}$ of 0‰. Values given in the figure are averages while errors given in figures are 1σ , apart from the Turrialba values in (C) which is the median; we do not use an average and a standard deviation for Turrialba due to the skewed distribution of the estimated slab fluid $\delta^{34}\text{S}$ in our Monte Carlo simulation.

We estimate a slab component with $\delta^{34}\text{S}$ between +2‰ and +5‰ is added to the mantle wedge under the CAVA. The highest estimate is for Turrialba calculated using a DMM mantle composition, which has a median value of +4.7‰. Using a PM mantle source at Turrialba, and assuming a chondritic $\delta^{34}\text{S}$ of 0‰ to demonstrate the effect of changing mantle $\delta^{34}\text{S}$, this value decreases to +2.7‰ (Fig. 10C). Slab component $\delta^{34}\text{S}$ is $+3.6 \pm 0.9$ ‰ at Cerro Negro, and 2.3 ± 1.7 ‰ at Fuego (1σ). These estimates would represent maximum $\delta^{34}\text{S}$ if total S loss is not achieved during melting, which may be the case under Fuego.

Estimates for the $\delta^{34}\text{S}$ value of the slab component derived from our model (+2 to +5‰) are lower than the estimate of +8‰ of de Moor et al. (2022) for the CAVA or the +5‰ to +9‰ estimate of Muth and Wallace (2021) for the Lassen complex, Cascadia. Pre-subduction mantle S contents above 200 ppm may require the slab component to have higher $\delta^{34}\text{S}$: however, a source that is more primitive (Herrstrom et al., 1995) or contains pyroxenite (Heydolph et al., 2012) will likely experience higher degrees of melting as well, and hence require a similar amount (or more) slab-derived S to be added to the wedge (Fig. 10). Inter-arc differences be-

tween the isotopic composition of slab-derived sulfur (Fig. 8) may relate to different slab thermal structure, sedimentary input, slab age, conversion rate, or the nature of the pre-subduction mantle source.

The modelled slab component $\delta^{34}\text{S}$ value for Turrialba (~+5‰) is higher than average input $\delta^{34}\text{S}$ estimates calculated for the Cocos-Nazca Ridge that subducts at Costa Rica (-0.2‰, Fig. 10C). It is also higher at Cerro Negro (+3.6 ± 0.9‰) than the East Pacific Rise (EPR) estimate of +1.5‰ (de Moor et al., 2022), which subducts along the Guatemalan to Nicaraguan segments of the CAVA. At Fuego the EPR and the slab component $\delta^{34}\text{S}$ values overlap (Fig. 10C). Our results suggest that sulfur isotopes can fractionate effectively in the slab during subduction, enriching slab fluids/melts in ^{34}S and causing preferential recycling of ^{32}S from the surface into the deep mantle. Fractionation during formation of the slab-derived component, such as preferential sulfur loss from sulfate-rich lithologies (Muth and Wallace, 2021), or through metamorphic reactions during the migration of fluids within the slab (Walters et al., 2019) are both plausible explanations. Over geological time both processes may play a key role in the enrichment

of surface reservoirs, such as the Earth's oceans, in ^{34}S (Canfield, 2004). While fractionation of S isotopes is not clearly evident under Fuego, the mantle wedge should be still enriched in ^{34}S by the slab component, relative to DMM. Based on currently available data on $\delta^{34}\text{S}$ variability within the subducting plate, which point to an overall enrichment of ^{34}S in oxidised phases such as sulfate (Alt and Shanks, 2003; Canfield, 2004; Alt et al., 2012), our results indicate that preferential mobilisation of oxidised, ^{34}S -rich sulfur from the subducting slab is necessary to achieve the positive $\delta^{34}\text{S}$ of the slab component and CAVA primary melts (Fig. 7 and 10). These processes are expected to oxidise primary arc magmas (Brounce et al., 2014). The sulfur isotope measurements from CAVA MIs together with similar measurements from the Cascades and Kyushu (Muth and Wallace, 2021; Kawaguchi et al., 2022) therefore offer strong evidence that the mobilisation of sulfate from the subducting slab plays a direct role in creating the characteristic oxidised signature of arc magmas compared to MORB settings.

6. Conclusions

Understanding sulfur cycling at subduction zones is key to elucidate the partitioning of this key element between Earth's surface and interior through geological time. Sulfur isotope analyses of melt inclusions and glasses from three volcanic centres in the Central American volcanic arc (CAVA) reveal ^{34}S enrichment in undegassed arc melts compared to MORBs. Undegassed CAVA magmas have S contents between 2700–3400 ppm and $\delta^{34}\text{S}$ between $+0.9 \pm 1.4\text{‰}$ (Fuego), $+2.2 \pm 1.0\text{‰}$ (Cerro Negro), and $+1.6 \pm 0.8\text{‰}$ at Turrialba (Costa Rica). Sulfur isotope ratio estimates of undegassed CAVA magmas overlap within uncertainty for the three studied volcanoes, despite the huge variations in trace element ratios sensitive to slab-mantle interaction (such as La/Ba) measured along the arc. Using mass balance calculations, we estimate that the mantle wedge likely contains more than 50% slab-derived S under the CAVA (Fig. 10B), dominating the sulfur budget of volcanic arcs. The slab-derived sulfur budget estimates overlap at the three studied locations. We estimate that the slab component has elevated $\delta^{34}\text{S}$ ($+2\text{‰}$ to $+5\text{‰}$) compared to estimates of subduction inputs along the CAVA (0 to $+1.5\text{‰}$), indicating enrichment of ^{34}S in slab fluids/melts compared subduction inputs. We anticipate ^{34}S to be enriched in mainly oxidised material (sulfates); formation of ^{34}S -rich fluids/melts may be best explained by the removal of oxidised material from the slab. These fluids/melts may ultimately contribute to oxidation within the mantle wedge and subsequently in arc magmas. The elevated $\delta^{34}\text{S}$ in arc magmas compared to mid-ocean ridge basalts is a global feature as demonstrated by our and other melt inclusion datasets (Muth and Wallace, 2021; Kawaguchi et al., 2022). Our results show that sulfur isotopes are powerful tracers of slab-mantle interaction at subduction zones and highlight the value of melt inclusions to constrain the evolution of sulfur in magmatic systems. Subduction zone processes potentially play a key role in governing the Earth's sulfur cycle, the evolution of sulfur isotope signature in different Earth-system reservoirs and the oxidation state of the Earth's mantle over its geological history.

CRediT authorship contribution statement

Z. Taracsák: Conceptualization, Formal analysis, Investigation, Methodology, Visualization, Writing – original draft, Writing – review & editing. **T.A. Mather:** Conceptualization, Funding acquisition, Resources, Supervision, Writing – review & editing. **S. Ding:** Conceptualization, Investigation, Writing – review & editing. **T. Plank:** Conceptualization, Funding acquisition, Resources, Writing – review & editing. **M. Brounce:** Formal analysis, Investigation, Writing – review & editing. **D.M. Pyle:** Conceptualization, Writing – review & editing. **A. Aiuppa:** Conceptualization, Writing – review & editing. **EIMF:** Formal analysis, Investigation.

Declaration of competing interest

The authors declare that they have no known competing financial interests or personal relationships that could have appeared to influence the work reported in this paper.

Data availability

We provide all the data used in this work as an electronic supplementary material.

Acknowledgements

Our work have been supported by NSFGE0-NERC grant “Sulfur cycling in subduction zones” awarded to TP (award no. 1933773) and TAM (NE/T010940/1). We acknowledge further support from NERC to use the Ion-probe facility in Edinburgh (grant no. IMF703-0520). We are extremely grateful to John Craven at EIMF who carried out our SIMS analyses and for providing remote access to the SIMS facility in Edinburgh during the UK-wide lockdown in late 2020 and early 2022. Furthermore, we thank Andrew Matzen (University of Oxford) for his valuable help with the EPMA analyses. We thank J. Maarten de Moor (Universidad Nacional de Costa Rica) for providing the Turrialba sample we used in this study, Bill Rose and Omar Flores for the Fuego samples, and Anna Barth for the Cerro Negro sample. We thank the two anonymous reviewers for their constructive and helpful comments, and Chiara Petrone for the editorial handling of our manuscript.

Appendix A. Supplementary material

Supplementary material related to this article can be found online at <https://doi.org/10.1016/j.epsl.2022.117948>.

References

- Alt, J.C., Garrido, C.J., Shanks, W.C.I., Turchyn, A., Padrón-Navarta, J.A., Sánchez-Vizcaíno, V.L., Pugnaire, M.T.G., Marchesi, C., 2012. Recycling of water, carbon, and sulfur during subduction of serpentinites: a stable isotope study of cerro del almirez, Spain. *Earth Planet. Sci. Lett.* 327, 50–60. <https://doi.org/10.1016/j.epsl.2012.01.029>.
- Alt, J.C., Shanks, W.C.I., 2003. Serpentinization of abyssal peridotites from the MARK area, Mid-Atlantic Ridge: sulfur geochemistry and reaction modeling. *Geochim. Cosmochim. Acta* 67 (4), 641–653. [https://doi.org/10.1016/S0016-7037\(02\)01142-0](https://doi.org/10.1016/S0016-7037(02)01142-0).
- Barth, A., Newcombe, M., Plank, T., Gonnermann, H., Hajimirza, S., Soto, G.J., Saballos, A., Hauri, E., 2019. Magma decompression rate correlates with explosivity at basaltic volcanoes—constraints from water diffusion in olivine. *J. Volcanol. Geotherm. Res.* 387, 106664. <https://doi.org/10.1016/j.jvolgeores.2019.106664>.
- Bekaert, D., Turner, S., Broadley, M., Barnes, J., Halldórsson, S., Labidi, J., Wade, J., Walowski, K., Barry, P., 2021. Subduction-driven volatile recycling: a global mass balance. *Annu. Rev. Earth Planet. Sci.* 49 (1), 37–70. <https://doi.org/10.1146/annurev-earth-071620-055024>.
- Benjamin, E.R., Plank, T., Wade, J.A., Kelley, K.A., Hauri, E.H., Alvarado, G.E., 2007. High water contents in basaltic magmas from Irazú Volcano, Costa Rica. *J. Volcanol. Geotherm. Res.* 168 (1–4), 68–92. <https://doi.org/10.1016/j.jvolgeores.2007.08.008>.
- Bolge, L.L., Carr, M.J., Milidakis, K.I., Lindsay, F.N., Feigenson, M.D., 2009. Correlating geochemistry, tectonics, and volcanic volume along the Central American volcanic front. *Geochem. Geophys. Geosyst.* 10 (12). <https://doi.org/10.1029/2009GC002704>.
- Brounce, M.N., Kelley, K.A., Cottrell, E., 2014. Variations in $\text{Fe}^{3+}/\Sigma\text{Fe}$ of Mariana arc basalts and mantle wedge fO₂. *J. Petrol.* 55, 2513–2536. <https://doi.org/10.1093/ptrology/egu065>.
- Bucholz, C.E., Gaetani, G.A., Behn, M.D., Shimizu, N., 2013. Post-entrapment modification of volatiles and oxygen fugacity in olivine-hosted melt inclusions. *Earth Planet. Sci. Lett.* 374, 145–155. <https://doi.org/10.1016/j.epsl.2013.05.033>.
- Burgisser, A., Alletti, M., Scaillet, B., 2015. Simulating the behavior of volatiles belonging to the C–O–H–S system in silicate melts under magmatic conditions with the software D-Compress. *Comput. Geosci.* 79, 1–14. <https://doi.org/10.1016/j.cageo.2015.03.002>.
- Canfield, D.E., 2004. The evolution of the Earth surface sulfur reservoir. *Am. J. Sci.* 304 (10), 839–861. <https://doi.org/10.2475/ajs.304.10.839>.

- Carr, M., Feigenson, M., Bolge, L., Walker, J., Gazel, E., 2015. RU_CAGeochem v. 4, a database and sample repository for Central American volcanic rocks at Rutgers University. Interdisciplinary Earth Data Alliance (IEDA). <https://doi.org/10.1002/gdj3.10>, Version 1.0. (Accessed 10 February 2021).
- Chowdhury, P., Dasgupta, R., 2019. Effect of sulfate on the basaltic liquidus and Sulfur Concentration at Anhydrite Saturation (SCAS) of hydrous basalts – implications for sulfur cycle in subduction zones. *Chem. Geol.* 522, 162–174. <https://doi.org/10.1016/j.chemgeo.2019.05.020>.
- Danyushevsky, L.V., McNeill, A.W., Sobolev, A.V., 2002. Experimental and petrological studies of melt inclusions in phenocrysts from mantle-derived magmas: an overview of techniques, advantages and complications. *Chem. Geol.* 183 (1–4), 5–24. [https://doi.org/10.1016/S0009-2541\(01\)00369-2](https://doi.org/10.1016/S0009-2541(01)00369-2).
- de Hoog, J., Taylor, B., van Bergen, M., 2001. Sulfur isotope systematics of basaltic lavas from Indonesia: implications for the sulfur cycle in subduction zones. *Earth Planet. Sci. Lett.* 189 (3), 237–252. [https://doi.org/10.1016/S0012-821X\(01\)00355-7](https://doi.org/10.1016/S0012-821X(01)00355-7).
- de Moor, J.M., Aiuppa, A., Averd, G., Wehrmann, H., Dunbar, N., Muller, C., Tamburillo, G., Giudice, G., Liuzzo, M., Moretti, R., et al., 2016. Turmoil at Turrialba Volcano (Costa Rica): degassing and eruptive processes inferred from high-frequency gas monitoring. *J. Geophys. Res., Solid Earth* 121 (8), 5761–5775. <https://doi.org/10.1002/2016JB013150>.
- de Moor, J.M., Fischer, T.P., Plank, T., 2022. Constraints on the sulfur subduction cycle in Central America from sulfur isotope compositions of volcanic gases. *Chem. Geol.* 588, 120627. <https://doi.org/10.1016/j.chemgeo.2021.120627>.
- de Moor, J.M., Fischer, T.P., Sharp, Z.D., Hauri, E.H., Hilton, D.R., Atudorei, V., 2010. Sulfur isotope fractionation during the May 2003 eruption of anatahan volcano, Mariana Islands: implications for sulfur sources and plume processes. *Geochim. Cosmochim. Acta* 74 (18), 5382–5397. <https://doi.org/10.1016/j.gca.2010.06.027>.
- DeVitre, C.L., Gazel, E., Allison, C.M., Soto, G., Madrigal, P., Alvarado, G.E., Lücke, O.H., 2019. Multi-stage chaotic magma mixing at Turrialba volcano. *J. Volcanol. Geotherm. Res.* 381, 330–346. <https://doi.org/10.1016/j.jvolgeores.2019.06.011>.
- Di Piazza, A., Rizzo, A., Barberi, F., Carapezza, M., De Astis, G., Romano, C., Sortino, F., 2015. Geochemistry of the mantle source and magma feeding system beneath Turrialba volcano, Costa Rica. *Lithos* 232, 319–335. <https://doi.org/10.1016/j.lithos.2015.07.012>.
- Ding, S., Dasgupta, R., 2017. The fate of sulfide during decompression melting of peridotite—implications for sulfur inventory of the morib-source depleted upper mantle. *Earth Planet. Sci. Lett.* 459, 183–195. <https://doi.org/10.1016/j.epsl.2016.11.020>.
- Edmonds, M., Liu, E., Cashman, K., 2022. Open-vent volcanoes fuelled by depth-integrated magma degassing. *Bull. Volcanol.* 84 (3), 1–27. <https://doi.org/10.1007/s00445-021-01522-8>.
- Evans, K., 2012. The redox budget of subduction zones. *Earth-Sci. Rev.* 113 (1), 11–32. <https://doi.org/10.1016/j.earscirev.2012.03.003>.
- Feigenson, M.D., Carr, M.J., 1986. Positively correlated Nd and Sr isotope ratios of lavas from the Central American volcanic front. *Geology* 14 (1), 79–82. [https://doi.org/10.1130/0091-7613\(1986\)14<79:PCNASI>2.0.CO;2](https://doi.org/10.1130/0091-7613(1986)14<79:PCNASI>2.0.CO;2).
- Fortin, M.-A., Riddle, J., Desjardins-Langlais, Y., Baker, D.R., 2015. The effect of water on the sulfur concentration at sulfide saturation (SCSS) in natural melts. *Geochim. Cosmochim. Acta* 160, 100–116. <https://doi.org/10.1016/j.gca.2015.03.022>.
- Gazel, E., Carr, M.J., Hoernle, K., Feigenson, M.D., Szymanski, D., Hauff, F., van den Bogaard, P., 2009. Galapagos-OIB signature in southern Central America: mantle refertilization by arc-hot spot interaction. *Geochim. Geophys. Geosyst.* 10 (2). <https://doi.org/10.1029/2008GC002246>.
- Gurenko, A.A., 2021. Origin of sulphur in relation to silicate-sulphide immiscibility in Tolbachik primitive arc magma (Kamchatka, Russia): insights from sulphur and boron isotopes. *Chem. Geol.* 576, 120244. <https://doi.org/10.1016/j.chemgeo.2021.120244>.
- Herrstrom, E.A., Reagan, M.K., Morris, J.D., 1995. Variations in lava composition associated with flow of asthenosphere beneath southern Central America. *Geology* 23 (7), 617–620. [https://doi.org/10.1130/0091-7613\(1995\)023<0617:VILCAW>2.3.CO;2](https://doi.org/10.1130/0091-7613(1995)023<0617:VILCAW>2.3.CO;2).
- Heydolph, K., Hoernle, K., Hauff, F., van den Bogaard, P., Portnyagin, M., Bindeman, I., Garbe-Schönberg, D., 2012. Along and across arc geochemical variations in NW Central America: evidence for involvement of lithospheric pyroxenite. *Geochim. Cosmochim. Acta* 84, 459–491. <https://doi.org/10.1016/j.gca.2012.01.035>.
- Hoernle, K., Abt, D.L., Fischer, K.M., Nichols, H., Hauff, F., Abers, G.A., Van Den Bogaard, P., Heydolph, K., Alvarado, G., Protti, M., et al., 2008. Arc-parallel flow in the mantle wedge beneath Costa Rica and Nicaragua. *Nature* 451 (7182), 1094–1097. <https://doi.org/10.1038/nature06550>.
- Jégo, S., Dasgupta, R., 2014. The fate of sulfur during fluid-present melting of subducting basaltic crust at variable oxygen fugacity. *J. Petrol.* 55 (6), 1019–1050. <https://doi.org/10.1093/petrology/egu016>.
- Jugo, P.J., Wilke, M., Botcharnikov, R.E., 2010. Sulfur K-edge XANES analysis of natural and synthetic basaltic glasses: implications for S speciation and S content as function of oxygen fugacity. *Geochim. Cosmochim. Acta* 74 (20), 5926–5938. <https://doi.org/10.1016/j.gca.2010.07.022>.
- Kawaguchi, M., Koga, K.T., Rose-Koga, E., Shimizu, K., Ushikubo, T., Yoshiasa, A., 2022. Sulfur isotope and trace element systematics in arc magmas: seeing through the degassing via a melt inclusion study of Kyushu Island volcanoes, Japan. *J. Petrol.* 63 (7), Egac061. <https://doi.org/10.1093/petrology/egac061>.
- Kelley, K.A., Plank, T., Grove, T.L., Stolper, E.M., Newman, S., Hauri, E., 2006. Mantle melting as a function of water content beneath back-arc basins. *J. Geophys. Res., Solid Earth* 111 (B9). <https://doi.org/10.1029/2005JB003732>.
- Labidi, J., Cartigny, P., Birc, J., Assayag, N., Bourrand, J., 2012. Determination of multiple sulfur isotopes in glasses: a reappraisal of the MORB $\delta^{34}\text{S}$. *Chem. Geol.* 334, 189–198. <https://doi.org/10.1016/j.chemgeo.2012.10.028>.
- Lee, C.-T.A., Erdman, M., Yang, W., Ingram, L., Chin, E.J., DePaolo, D.J., 2018. Sulfur isotopic compositions of deep arc cumulates. *Earth Planet. Sci. Lett.* 500, 76–85. <https://doi.org/10.1016/j.epsl.2018.08.017>.
- Lee, C.-T.A., Luffi, P., Chin, E.J., Bouchet, R., Dasgupta, R., Morton, D.M., Le Roux, V., Yin, Q.-Z., Jin, D., 2012. Copper systematics in arc magmas and implications for crust-mantle differentiation. *Science* 336 (6077), 64–68. <https://doi.org/10.1016/j.gca.2005.04.023>.
- Leeman, W.P., Carr, M.J., Morris, J.D., 1994. Boron geochemistry of the Central American volcanic arc: constraints on the genesis of subduction-related magmas. *Geochim. Cosmochim. Acta* 58 (1), 149–168. [https://doi.org/10.1016/0016-7037\(94\)90453-7](https://doi.org/10.1016/0016-7037(94)90453-7).
- Lloyd, A.S., Plank, T., Ruprecht, P., Hauri, E.H., Rose, W., 2013. Volatile loss from melt inclusions in pyroclasts of differing sizes. *Contrib. Mineral. Petrol.* 165 (1), 129–153. <https://doi.org/10.1007/s00410-012-0800-2>.
- MacLennan, J., 2017. Bubble formation and decrepitation control the CO_2 content of olivine-hosted melt inclusions. *Geochim. Geophys. Geosyst.* 18, 597–616. <https://doi.org/10.1002/2016GC006633>.
- Marini, L., Moretti, R., Accornero, M., 2011. Sulfur isotopes in magmatic-hydrothermal systems, melts, and magmas. *Rev. Mineral. Geochem.* 73 (1), 423–492. <https://doi.org/10.2138/rmg.2011.73.14>.
- Mironov, N., Portnyagin, M., Botcharnikov, R., Gurenko, A., Hoernle, K., Holtz, F., 2015. Quantification of the CO_2 budget and H_2O – CO_2 systematics in subduction-zone magmas through the experimental hydration of melt inclusions in olivine at high H_2O pressure. *Earth Planet. Sci. Lett.* 425, 1–11. <https://doi.org/10.1016/j.epsl.2015.05.043>.
- Müller, R.D., Sdrólías, M., Gaina, C., Roest, W.R., 2008. Age, spreading rates, and spreading asymmetry of the world's ocean crust. *Geochim. Geophys. Geosyst.* 9 (4). <https://doi.org/10.1029/2007GC001743>.
- Métrich, N., Schiano, P., Clochiatti, R., Maury, R.C., 1999. Transfer of sulfur in subduction settings: an example from Batán Island (Luzon volcanic arc, Philippines). *Earth Planet. Sci. Lett.* 167 (1), 1–14. [https://doi.org/10.1016/S0012-821X\(99\)00009-6](https://doi.org/10.1016/S0012-821X(99)00009-6).
- Mungall, J.E., 2002. Roasting the mantle: slab melting and the genesis of major Au and Au-rich Cu deposits. *Geology* 30 (10), 915–918. [https://doi.org/10.1130/0091-7613\(2002\)030<0915:RTMSMA>2.0.CO;2](https://doi.org/10.1130/0091-7613(2002)030<0915:RTMSMA>2.0.CO;2).
- Muth, M.J., Wallace, P.J., 2021. Slab-derived sulfate generates oxidized basaltic magmas in the southern Cascade arc (California, USA). *Geology* 06. <https://doi.org/10.1130/G48759.1>.
- Muth, M.J., Wallace, P.J., 2022. Sulfur recycling in subduction zones and the oxygen fugacity of mafic arc magmas. *Earth Planet. Sci. Lett.* 599, 117836. <https://doi.org/10.1016/j.epsl.2022.117836>.
- Nash, W.M., Smythe, D.J., Wood, B.J., 2019. Compositional and temperature effects on sulfur speciation and solubility in silicate melts. *Earth Planet. Sci. Lett.* 507, 187–198. <https://doi.org/10.1016/j.epsl.2018.12.006>.
- O'Neill, H.S.C., Berry, A.J., Mallmann, G., 2018. The oxidation state of iron in Mid-Ocean Ridge Basaltic (MORB) glasses: implications for their petrogenesis and oxygen fugacities. *Earth Planet. Sci. Lett.* 504, 152–162. <https://doi.org/10.1016/j.epsl.2018.10.002>.
- Patino, L.C., Carr, M.J., Feigenson, M.D., 2000. Local and regional variations in Central American arc lavas controlled by variations in subducted sediment input. *Contrib. Mineral. Petrol.* 138 (3), 265–283. <https://doi.org/10.1007/s004100050562>.
- Piccoli, F., Hermann, J., Pettker, T., Connolly, J., Kempf, E.D., Vieira Duarte, J.F., 2019. Subducting serpentinites release reduced, not oxidized, aqueous fluids. *Sci. Rep.* 9 (1), 1–7. <https://doi.org/10.1038/s41598-019-55944-8>.
- Plank, T., 2005. Constraints from thorium/lanthanum on sediment recycling at subduction zones and the evolution of the continents. *J. Petrol.* 46 (5), 921–944. <https://doi.org/10.1093/petrology/egi005>.
- Plank, T., Kelley, K.A., Zimmer, M.M., Hauri, E.H., Wallace, P.J., 2013. Why do mafic arc magmas contain ~4wt% water on average? *Earth Planet. Sci. Lett.* 364, 168–179. <https://doi.org/10.1016/j.epsl.2012.11.044>.
- Putirka, K.D., 2008. Thermometers and barometers for volcanic systems. *Rev. Mineral. Geochem.* 69 (1), 61–120. <https://doi.org/10.2138/rmg.2008.69.3>.
- Rasmussen, D.J., Plank, T.A., Wallace, P.J., Newcombe, M.E., Lowenstern, J.B., 2020. Vapor-bubble growth in olivine-hosted melt inclusions. *Am. Mineral.* 105 (12), 1898–1919. <https://doi.org/10.2138/am-2020-7777>.
- Reagan, M., Duarte, E., Soto, G.J., Fernández, E., 2006. The eruptive history of Turrialba volcano, Costa Rica, and potential hazards from future eruptions. *Spec. Pap., Geol. Soc. Am.* 412, 235. [https://doi.org/10.1130/2006.2412\(13\)](https://doi.org/10.1130/2006.2412(13)).
- Reagan, M.K., Gill, J.B., 1989. Coexisting calcalkaline and high-niobium basalts from Turrialba Volcano, Costa Rica: implications for residual titanates in arc magma sources. *J. Geophys. Res., Solid Earth* 94 (B4), 4619–4633. <https://doi.org/10.1029/JB094iB04p04619>.

- Ripley, B.D., Thompson, M., 1987. Regression techniques for the detection of analytical bias. *Analyst* 112, 377–383. <https://doi.org/10.1039/AN9871200377>.
- Ruscitto, D.M., Wallace, P.J., Cooper, L.B., Plank, T., 2012. Global variations in H₂O/Ce: 2. Relationships to arc magma geochemistry and volatile fluxes. *Geochem. Geophys. Geosyst.* 13 (3). <https://doi.org/10.1029/2011GC003887>.
- Sadofsky, S.J., Portnyagin, M., Hoernle, K., van den Bogaard, P., 2008. Subduction cycling of volatiles and trace elements through the Central American volcanic arc: evidence from melt inclusions. *Contrib. Mineral. Petrol.* 155 (4), 433–456. <https://doi.org/10.1007/s00410-007-0251-3>.
- Sakai, H., Casadevall, T.J., Moore, J.G., 1982. Chemistry and isotope ratios of sulfur in basalts and volcanic gases at Kilauea Volcano, Hawaii. *Geochim. Cosmochim. Acta* 46 (5), 729–738. [https://doi.org/10.1016/0016-7037\(82\)90024-2](https://doi.org/10.1016/0016-7037(82)90024-2).
- Salter, V.J.M., Stracke, A., 2004. Composition of the depleted mantle. *Geochem. Geophys. Geosyst.* 5 (5). <https://doi.org/10.1029/2003GC000597>.
- Schiavi, F., Bolfan-Casanova, N., Buso, R., Laumonier, M., Laporte, D., Medjoubi, K., Venugopal, S., Gómez-Ulla, A., Cluzel, N., Hardiagon, M., 2020. Quantifying magmatic volatiles by Raman microtomography of glass inclusion-hosted bubbles. *Geochem. Perspect. Lett.* 16, 17–24. <https://doi.org/10.7185/geochemlet.2038>.
- Schmidt, M., Poli, S., 2014. 4.19 - devolatilization during subduction. In: Holland, H.D., Turekian, K.K. (Eds.), *Treatise on Geochemistry*, second edition. Elsevier, Oxford, pp. 669–701.
- Shi, S., Barth, A., Plank, T., Towbin, W., Omar, F., Arias, C., 2021. Magma stalling weakens eruption. In: *AGU Fall Meeting Abstracts*, vol. 2021. pp. V25E–09.
- Stolper, D.A., Bucholz, C.E., 2019. Neoproterozoic to early Phanerozoic rise in island arc redox state due to deep ocean oxygenation and increased marine sulfate levels. *Proc. Natl. Acad. Sci.* 116 (18), 8746–8755. <https://doi.org/10.1073/pnas.1821847116>.
- Stolper, D.A., Higgins, J.A., Derry, L.A., 2021. The role of the solid earth in regulating atmospheric O₂ levels. *Am. J. Sci.* 321 (10), 1381–1444. <https://doi.org/10.2475/10.2021.01>.
- Syracuse, E.M., van Keken, P.E., Abers, G.A., 2010. The global range of subduction zone thermal models. *Phys. Earth Planet. Inter.* 183 (1), 73–90. <https://doi.org/10.1016/j.pepi.2010.02.004>. special Issue on Deep Slab and Mantle Dynamics.
- Taracsák, Z., Neave, D., Beaudry, P., Gunnarsson-Robin, J., Burgess, R., Edmonds, M., Halldórsson, S., Longpré, M.-A., Ono, S., Ranta, E., Stefánsson, A., Turchyn, A., EIMF, Hartley, M., 2021. Instrumental mass fractionation during sulfur isotope analysis by secondary ion mass spectrometry in natural and synthetic glasses. *Chem. Geol.* 578, 120318. <https://doi.org/10.1016/j.chemgeo.2021.120318>.
- Tassara, S., Reich, M., Cannatelli, C., Konecke, B., Kausel, D., Morata, D., Barra, F., Simon, A., Fiege, A., Morgado, E., Leisen, M., 2020. Post-melting oxidation of highly primitive basalts from the southern Andes. *Geochim. Cosmochim. Acta* 273, 291–312. <https://doi.org/10.1016/j.gca.2020.01.042>.
- Tollan, P., Hermann, J., 2019. Arc magmas oxidized by water dissociation and hydrogen incorporation in orthopyroxene. *Nat. Geosci.* 12 (8), 667–671. <https://doi.org/10.1038/s41561-019-0411-x>.
- Turner, S., Hoernle, K., Hauff, F., Johansen, T.S., Klügel, A., Kokfelt, T., Lundstrom, C., 2015. ²³⁸U – ²³⁰Th – ²²⁶Ra Disequilibria Constraints on the Magmatic Evolution of the Cumbre Vieja Volcanics on La Palma, Canary Islands. *J. Petrol.* 56 (10), 1999–2024. <https://doi.org/10.1093/petrology/egv061>.
- Walters, J., Cruz-Urbe, A., Marschall, H., 2020. Sulfur loss from subducted altered oceanic crust and implications for mantle oxidation. *Geochem. Perspect. Lett.* 13, 36–41. <https://doi.org/10.7185/geochemlet.2011>.
- Walters, J.B., Cruz-Urbe, A.M., Marschall, H.R., 2019. Isotopic compositions of sulfides in exhumed high-pressure terranes: implications for sulfur cycling in subduction zones. *Geochem. Geophys. Geosyst.* 20 (7), 3347–3374. <https://doi.org/10.1029/2019GC008374>.
- Zajacz, Z., Tsay, A., 2019. An accurate model to predict sulfur concentration at anhydrite saturation in silicate melts. *Geochim. Cosmochim. Acta* 261, 288–304. <https://doi.org/10.1016/j.gca.2019.07.007>.
- Zhao, S.-Y., Yang, A.Y., Langmuir, C.H., Zhao, T.-P., 2022. Oxidized primary arc magmas: constraints from Cu/Zr systematics in global arc volcanics. *Sci. Adv.* 8 (12), eabk0718. <https://doi.org/10.1126/sciadv.abk0718>.